






Article

SAR-AD Method to Characterize Eight SARA Fractions in Various Vacuum Residues and Follow Their Transformations Occurring during Hydrocracking and Pyrolysis

Jeramie J. Adams ^{1,*} , Joseph F. Rovani ¹, Jean-Pascal Planche ¹, Jenny Loveridge ¹, Alex Literati ¹, Ivelina Shishkova ² , Georgi Palichev ³, Iliyan Kolev ^{2,3}, Krassimir Atanassov ^{3,4} , Svetoslav Nenov ⁵, Simeon Ribagin ³, Danail Stratiev ³, Dobromir Yordanov ⁴  and Jianqiang Huo ⁶ 

¹ Western Research Institute, Laramie, WY 82072, USA

² LUKOIL Neftohim Burgas, 8104 Burgas, Bulgaria

³ Institute of Biophysics and Biomedical Engineering, Bulgarian Academy of Sciences, Academic Georgi Bonchev 105, 1113 Sofia, Bulgaria

⁴ Department of Industrial Technologies and Management, University Prof. Dr. Assen Zlatarov, Professor Yakimov 1, 8010 Burgas, Bulgaria

⁵ Department of Mathematics, University of Chemical Technology and Metallurgy, Kliment Ohridski 8, 1756 Sofia, Bulgaria

⁶ Department of Chemical Engineering, University of Wyoming, 1000 E University Avenue, Laramie, WY 82071, USA

* Correspondence: jadams32@uwyo.edu



Citation: Adams, J.J.; Rovani, J.F.; Planche, J.-P.; Loveridge, J.; Literati, A.; Shishkova, I.; Palichev, G.; Kolev, I.; Atanassov, K.; Nenov, S.; et al. SAR-AD Method to Characterize Eight SARA Fractions in Various Vacuum Residues and Follow Their Transformations Occurring during Hydrocracking and Pyrolysis. *Processes* **2023**, *11*, 1220. <https://doi.org/10.3390/pr11041220>

Academic Editor: Miguel Ladero Galán

Received: 6 March 2023

Revised: 24 March 2023

Accepted: 6 April 2023

Published: 15 April 2023



Copyright: © 2023 by the authors. Licensee MDPI, Basel, Switzerland. This article is an open access article distributed under the terms and conditions of the Creative Commons Attribution (CC BY) license (<https://creativecommons.org/licenses/by/4.0/>).

Abstract: Model compounds were used to provide some chemical boundaries for the eight-fraction SAR-ADTM characterization method for heavy oils. It was found that the Saturates fraction consists of linear and highly cyclic alkanes; the Aro-1 fraction consists of molecules with a single aromatic ring; the Aro-2 fraction consists of mostly 2 and 3-ring fused aromatic molecules, the pericondensed 4-ring molecule pyrene, and molecules with 3–5 rings that are not fused; and the Aro-3 fraction consists of 4-membered linear and catacondensed aromatics, larger pericondensed aromatics, and large polycyclic aromatic hydrocarbons. The Resins fraction consists of mostly fused aromatic ring systems containing polar functional groups and metallated polar vanadium oxide porphyrin compounds, and the Asphaltene fraction consists of both island- and archipelago-type structures with a broad range of molecular weight variation, aromaticity, and heteroatom contents. The behavior of the eight SAR-ADTM fractions during hydrocracking and pyrolysis was investigated, and quantitative relations were established. Intercriteria analysis and evaluation of SAR-ADTM data of hydrocracked vacuum residue and sediment formation rate in commercial ebullated bed vacuum residue hydrocracking were performed. It showed that total asphaltene content, toluene-soluble asphaltenes, and colloidal instability index contribute to sediment formation, while Resins and Cyclohexane-soluble asphaltenes had no statistically meaningful relation to sediment formation for the studied range of operation conditions.

Keywords: vacuum residue; hydrocracking; SARA composition; SAR-AD; asphaltene solubility profile; intercriteria analysis

1. Introduction

Feedstock selection is the critical primary factor influencing most profitable petroleum refining processes. Vacuum residue feedstock characterization is of pivotal importance for bottom of the barrel hydrocracking upgrading processes [1–5]. The characterization of the vacuum residues is not trivial due to their low volatility, high melting point, and extremely complex composition. More than 95% of the molecules have never been isolated or identified from vacuum residues and thus remain unknown [6]. The typical characterization of the petroleum distillates (that includes boiling point distribution and density,

allowing prediction of some important structure parameters) is not feasible for the vacuum residual oils due to their low volatility [7]. This has motivated researchers to devise methods to quantify similar classes of compounds using the saturates, aromatics, resins, and asphaltenes (SARA) composition analysis [8]. These analyses have provided an effective method to understand some aspects of bottom of the barrel upgrading processes [3,9–25].

Throughout the years, different methodologies have been developed to perform SARA analysis [26–48]. In general, the SARA analysis methodologies applied by different researchers can be divided into three main groups of chromatographic platforms: liquid chromatography, thin layer chromatography/flame ionization detection (TLC/FID), and high-performance liquid chromatography (HPLC) [42]. However, differences in the chromatographic platforms, sample preparation used for various methods can vary significantly, and methodologies can vary by utilizing different sorbent and solvent phases. With respect to sample preparation, some methods perform the asphaltene separation prior to chromatographing the maltenes (SAR fractions). This is generally favored since a significant portion of asphaltenes become irreversibly adsorbed to the sorbent phase, which can change the sorbent's activity. As an added layer of complexity, there are various solvents that can be used to precipitate asphaltenes, which will affect the quantity of resins and asphaltenes. In general, smaller alkyl chain solvents precipitate more asphaltenes than longer alkyl chain solvents, e.g., pentane vs. heptane, and branched lower solubility parameter solvents like isooctane can precipitate more asphaltenes relative to more linear alkane isomers. Other methods allow for in situ analysis for quantification of the SAR fractions and asphaltenes for the whole residue. Aside from sample preparation, the other dominant factor that affects the SAR separation is the sorbent and solvent systems used to perform the chromatography. Different sorbent and solvent combinations affect the cut points and overlap in molecular species during chromatography. As a result, data obtained from the same samples in different laboratories that employ different SARA techniques can be extremely variable, making it extremely difficult to draw universal conclusions from SARA data from different laboratories [41,49]. Nevertheless, the SARA techniques do provide a relatively complete characterization compared to individual molecular identification of the vacuum residue and are useful for characterizing feedstocks for bottom of the barrel upgrading processes [3,19,24,25].

For more sophisticated SARA separations, Liang et al. [27] proposed an eight group-fraction separation method that further separated aromatics and resins into light, middle, and heavy fractions, respectively [27]. Zhang et al. [23] employed the eight group-fraction SARA separation method to investigate the coking tendency of the eight group-fractions of Iranian vacuum residue. Che et al. [24] employed the eight group-fraction SARA separation method to investigate the pyrolysis behaviors and kinetics of the eight group-fractions, showing that each fraction has individual cracking pathways, which are determined by the chemical nature of the constituents. Zhang et al. [25] investigated the millisecond pyrolysis behavior of the eight group-fractions of Changqing vacuum residue. Their results showed that the eight group-fractions from saturate to asphaltene showed different compositions and structures, which provided valuable, more in-depth information for understanding the structure of heavy oil. Due to this difference in composition and structure, the eight group-fractions showed different cracking behaviors [25]. Within the portfolio of more advanced separations is the Western Research Institute-developed SAR-ADTM separation method [39,40]. In the SAR-AD separation, five distinct maltene fractions (Saturates, Aromatics (Aro-1, Aro-2, Aro-3), and Resins) are obtained by chromatography, and three different asphaltene subfractions are obtained by solubility using three different solvents of increasing solvent power: cyclohexane, toluene, and dichloromethane:methanol (98:2 vol:vol) [50,51]. For simplicity, the cyclohexane-soluble asphaltenes are denoted as CyC_6 and the dichloromethane-soluble asphaltenes are denoted CH_2Cl_2 . The separation uses an evaporative light scattering detector (ELSD), which provides data similar to gravimetric weight percent, and a variable wavelength detector that measures the concentration of brown colored molecules that absorb light at 500 nm. The Asphaltene Determinator (AD)

portion of the separation was initially developed with U.S. Department of Energy and petroleum industry partner funding to quantify and monitor pyrolysis tolerance and coking onsets of heavy oils and bitumen. It was observed that as bitumen undergoes pyrolysis/cracking/visbreaking (thermal bond breaking), the free solvent volume of the asphaltenes decreases. The free solvent volume was found to be directly related to the amount of C_{10} asphaltenes [52], which systematically decreased with pyrolysis severity. As the C_{10} asphaltenes decrease, the more polar/less soluble pre-coke CH_2Cl_2 asphaltenes increase. By taking a ratio of these two asphaltene subfractions, a robust Coking Index was developed that is highly sensitive to the pyrolysis history and can predict the onset of coke particle formation [51]. For most bitumen, the Coking Index is between 3 and 16. For visbroken and hydrocracked materials, the Coking Index falls below 3 and can become significantly lower depending upon the severity of the conversion.

In recent studies, we investigated the ebullated bed vacuum residue hydrocracking performance employing the more traditional four-fraction SARA method for feed and hydrocracked vacuum residue characterization [53]. No reports were found in the literature studying ebullated bed vacuum residue hydrocracking performance with feed and hydrocracked vacuum residue characterization by the eight group SARA fractionation methods. Therefore, SAR-AD characterization of different straight-run vacuum residues derived from extra-light, light, medium, heavy, and extra-heavy crude oils from all over the world is included, including hydrocracked vacuum residues obtained at the conversion range of 55–91%. Nineteen individual vacuum residues derived from crude oils from Russia, Saudi Arabia, Iraq, Libya, Tunisia, Kazakhstan, Greece, Italy, Venezuela, Azerbaijan, and Albania, six blended vacuum residues available as feeds for processing in a commercial ebullated bed vacuum residue hydrocracker, and nine hydrocracked vacuum residues were characterized for this work.

The aim of this work is to study the eight SAR-AD fractions during hydrocracking of different vacuum residues and to establish a model for the quantitative relationship between the feedstock SAR-AD fraction contents and other common feed characterization data with relation to the performance of a commercial ebullated bed vacuum residue hydrocracker. A chemical understanding of the types of molecules that report to the various SAR-AD fractions, using various model compounds, helped to explain some of the trends and relationships for the feeds and products.

2. Materials and Methods

The properties of the nineteen studied crude oils and derived vacuum residues were characterized for their bulk density (ASTM D 4052), sulfur content (ASTM D 4294), Conradson carbon content (ASTM D 189), and vacuum residue SARA composition, performed according to the methodology developed in the LUKOIL Neftohim Burgas (LNB) Research Laboratory [36]. These data are summarized in Table 1. The data in Table 1 also includes the content of the vacuum residue fraction of the studied crude oils, determined by the use of a true boiling point (TBP) apparatus operating under the requirements of ASTM D 2892 for the atmospheric part and ASTM D 5236 for the vacuum part. The T50% of the crude oils was determined by the use of high temperature simulated distillation (HTSD) in accordance with the ASTM D 7169 standard.

The determination of softening point, T50% of the VRs, VR molecular weight, and viscosity of blends of the 19 studied vacuum residues (VR) with fluid catalytic cracking heavy cycle oil at a ratio of 70% VR/30% FCC HCO is described in our other recent research [54].

This investigation was performed at the commercial LNB H-Oil vacuum residue hydrocracker. A process diagram of the LNB H-Oil unit and the operating conditions employed at the LNB H-Oil hydrocracker are presented in our earlier studies [53,55,56].

Table 1. Physicochemical properties of studied crude oils and vacuum residue fractions derived thereof.

Nr	1	2	3	4	5	6	7	8	9	10	11	12	13	14	15	16	17	18	19
Crude type	Urals1	Urals2	Arab Med.	Arab Heavy	Basrah L	Basrah H	Kirkuk	El Bouri	CPC	LSCO	Prinos	Boscan	Varandey	Albania	Tempa Rossa	Rhemoura	Arab Light	Azeri Light	Imported AR
Crude D15. g/cm ³	0.877	0.875	0.872	0.889	0.878	0.905	0.873	0.891	0.805	0.854	0.875	1.002	0.85	1.001	0.94	0.865	0.858	0.848	
Crude Sulfur. wt. %	1.53	1.39	2.48	2.91	2.85	3.86	2.65	1.76	0.63	0.57	3.71	5.5	0.63	5.64	5.35	0.75	1.89	0.2	
Crude VR. wt. %	25.2	29	25.2	32	28.3	33.8	24.6	26.2	9.3	18.7	20.3	63.1	14.9	48.2	37.6	20.2	22.9	14.8	
Crude T50%. °C	378	380	376	429	392	418	345	401	238	352	349	571	362	531	428	350	352	321	
VR D15. g/cm ³	0.997	0.995	1.031	1.04	1.052	1.071	1.054	1.05	0.956	0.993	1.108	1.078	0.99	1.094	1.12	1.041	1.029	0.967	1.029
VR CCR. wt. %	17.5	17.0	20.7	23.6	23.8	28.9	25.2	25.5	16	14	32.8	27.8	15.1	31.4	34.3	23.7	18.7	9.5	19.2
VR Sulfur. wt. %	3.0	2.9	5.4	5.8	5.9	7.1	5.9	3.3	2.1	1.58	9.14	6	1.7	8.7	9.3	1.8	4.9	0.5	3.28
VR Sat. wt. %	25.6	22.9	11.8	12.4	12.3	12.3	15.2	12	44.6	25	12.6	15.1	33.5	10	2.2	19.7	15.9	40.2	17.5
VR Aro. wt. %	52.5	66.5	68.3	61.9	64.8	54.1	55.4	57.9	40.8	61.1	50.6	44.5	47.6	52.9	48.4	49.8	64.7	50.1	60.7
VR Res. wt. %	7.8	4.9	5.3	4.4	4.9	5.8	5	12.6	10.3	6.1	6.8	5.3	11.3	6.3	12.6	7.3	7.3	8.4	8.0
VR C ₇ asp. wt. %	14.1	6.3	14.6	21.3	18	27.7	24.3	17.5	3.4	7.8	30	35.2	7.6	37.7	36.8	23.2	12.1	1.4	13.7
VR C ₅ asp. wt. %	17.6	13.9	25.5	32.9	27.7	37	33.1	27.3	11	15.5	38.8	41	13.5	49.7	46.8	31.3	18.8	5.4	21.8
VR VIS. mm ² /s *	220.9		338.3	374.6	368.9	731.9	514.1	303	65	149.1	550	1003	103	680	759.5	255	192	77	
VR Softening point. °C	40.1	42.4	44.7	51.2	50.3	68.6	58.1	45	25.2	28.9	69.2	115	43.8	92.2	100	51.1	32.3	30.2	
VR T50%. °C	657		670	709	684	715	676	666	637	631	645	812	621	732	708	642	647	627	
MW. g/mol	808		840	953	877	968	853	827	757	741	760	1330	717	1017	931	766	778	731	

Note: D15 = density at 15 °C; VR = vacuum residue fraction; CCR = Conradson carbon content; Sat. = Saturates; Aro = Aromatics; Res. = Resins; C₇ asp. = n-heptane asphaltenes; C₅ asp. = n-pentane asphaltenes; VIS = kin. viscosity at 80 °C of the blend 70% VR/30% fluid catalytic cracking heavy cycle oil; Crude T50% = boiling point of 50% of the evaporate from the crude oil; VR T50% = boiling point of 50% of the evaporate from the vacuum residue fraction. * The viscosity values are related to the viscosity at 80 °C of mixtures of vacuum residues with fluid catalytic cracking heavy cycle oil, which has a viscosity at 80 °C of 4.4 mm²/s.

The SAR-AD method was performed according to the literature [39,40]. The dual-detector SAR-AD chromatograms obtained for a Lloydminster vacuum residue are shown in Figure 1.

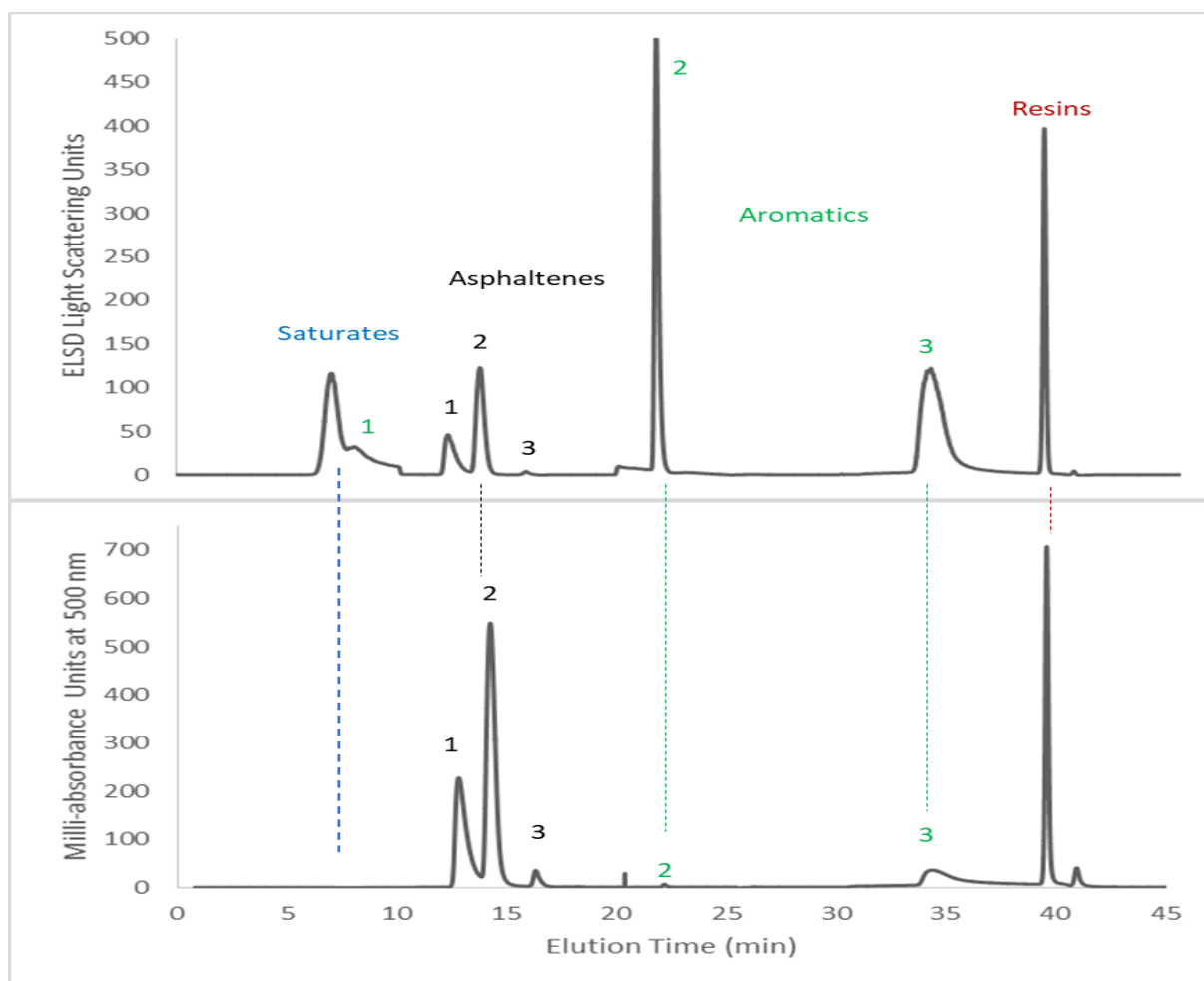


Figure 1. SAR-AD separation profiles for a Lloydminster vacuum residue. Asphaltene 1 = C_{10}H_8 , asphaltene 2 = Toluene, and Asphaltene 3 = CH_2Cl_2 . (The different colors designate Saturates—blue; Asphaltenes—black; Aromatics—green; Resins—red.)

The top chromatogram in Figure 1 is obtained using an evaporative light scattering detector, which gives an approximate weight percent as long as molecules are heavy enough to remain during the solvent evaporation process. The bottom chromatogram is collected using a variable wavelength or diode array detector set at 500 nm to give the concentration of brown colored material in the sample. The SAR-AD instrument contains both detectors, with the 500 nm detector configured immediately before the ELSD.

The Saturates fraction elutes first in the separation as non-adsorbed molecules flowing through four analytical columns. These molecules include fully saturated alkyl molecules, including cyclic (naphthenic) hydrocarbon molecules. It is the most hydrogen-rich non-polar fraction in the bitumen chemistry spectrum. The Aro-1 fraction contains hydrocarbons with a single isolated aromatic ring with significant amounts of alkyl side chain branching, which may also contain cyclic moieties. Molecules in this fraction are a bit more polar in the solubility/polarity spectrum than those in the Saturates fraction. The Aro-2 fraction generally contains two–three aromatic rings, 4 or 5 ring molecules, and a limited amount of cyclic heteroatom-containing compounds (sulfur, nitrogen, and oxygen). Aro-3 contains primarily molecules with four or more aromatic rings and has increased heteroatom contents, which can consist of heterocyclic N-H, aromatic acyl, NH_2 , and aliphatic O-H

species. The Resins fraction consists of increasingly polar molecules, mainly attributed to polar heteroatom functional groups and fused aromatic ring systems. Resins are the most polar fraction of the maltenes. The CyC₆ asphaltenes consist of alkyl-substituted multi-aromatic core compounds with heteroatoms. Toluene asphaltenes are more polar due to either increased heteroatom polarity, number of heteroatoms, ability to aggregate more efficiently, and/or increased aromaticity. Finally, the CH₂Cl₂ asphaltenes are the most polar of the bitumen fractions, consisting of either the greatest amount of polar functional groups containing highly polar functional groups and/or the least amount of alkyl side chains. During pyrolysis, increasing amounts of CH₂Cl₂ asphaltenes are produced from other molecules and preclude the onset of coke formation, so in this case, they may be considered as highly aromatic pre-coke molecules. CH₂Cl₂ asphaltenes can be chemically different depending on their isolation method (e.g., from emulsion interfaces or from extrography) or petroleum treatment method (e.g., asphaltenes produced upon oxidation of petroleum have a higher amount of oxygen functional groups) from CH₂Cl₂ asphaltenes produced upon pyrolysis.

Model compounds were evaluated to establish some chemical boundaries for the SAR-AD bitumen fractions. Model compounds were purchased from Sigma-Aldrich St. Louis, Missouri, USA or TCI Chemicals, Portland, OR, USA and 1,3-bis-(1-pyrene) propane was purchased from Setareh Biotech, Eugene, OR, USA. For the volatile model compounds, which are not significantly detected in the ELSD and do not absorb at 500 nm, a diode array detector set to 290 nm was used. This allowed for the detection of molecules with at least two fused aromatic rings with virtually no overlap from toluene, which is the mobile phase used to elute two of the fractions. Absorbance at 290 nm was utilized to detect naphthalene; 2,6-diethylnaphthalene; 2,6-diisopropylnaphthalene; 2,6-ditertbutylnaphthalene; acenaphthylene; phenanthrene; 9,10-dihydrophenanthrene; binaphthalene; and indole. Model compound sample solutions were prepared at 2 percent *wt/vol* in chlorobenzene for injection. All solvents used were HPLC-grade. ELSD or 290 nm data were blank subtracted, and the areas were integrated according to the elution times used to define the fractions, as shown in Figure 1.

A quality control Lloydminster vacuum residue was used at the beginning and end of every sample sequence, and quality control was run after every 5 samples in sample sequences greater than 6 samples to ensure the quality of the separation. The standard deviation for the various fractions of the QC over the course of 10 days was 0.35 for Saturates, 0.50 for Aro-1, 0.69 for Aro-2, 0.90 for Aro-3, 0.58 for Resins, 0.28 for CyC₆ asphaltenes, 0.18 for Toluene asphaltenes, and 0.10 for CH₂Cl₂ asphaltenes.

Reference petroleum porphyrins were isolated from a Peace River bitumen by extracting with acetonitrile and removing the solvent under rotary evaporation. The extracts were then dissolved in heptane and separated chromatographically on activated Davisil 646 grade silica gel (Sigma Aldrich) using toluene as the eluent. The major porphyrin fraction was eluted as a bright red band. The porphyrin signature was determined using UV-Visible spectroscopy, which showed a strong Soret band at 410 nm and Q bands between 500 and 600 nm [57]. Figure 2 shows the elution of the porphyrins, the porphyrins after solvent removal, and the UV-Visible spectrum. Several useful metrics can be calculated from the SAR-AD fractions. The ratio between the CyC₆ and CH₂Cl₂ asphaltenes is a sensitive indicator for pyrolysis severity and is referred to as the Coking Index. It shows the buildup of the least-soluble asphaltenes (the most problematic asphaltenes) relative to the most-soluble asphaltenes and is directly related to how close the residue is to forming coke particles [50,51]. The initial motivation to separate and quantify CyC₆ asphaltenes was to approximate the free solvent volume relative to the total asphaltenes. The free solvent volume represents how much cracking the residue can undergo before forming coke [52,58]. Another useful metric for refinement is the colloidal instability index (CII). This is the ratio of the incompatible phases (Saturates + Aro-1 and Total Asphaltenes [CyC₆ + Toluene + CH₂Cl₂]) to the dissolving/dispersing phase (Aro-2 + Aro-3 + Resins) [38].

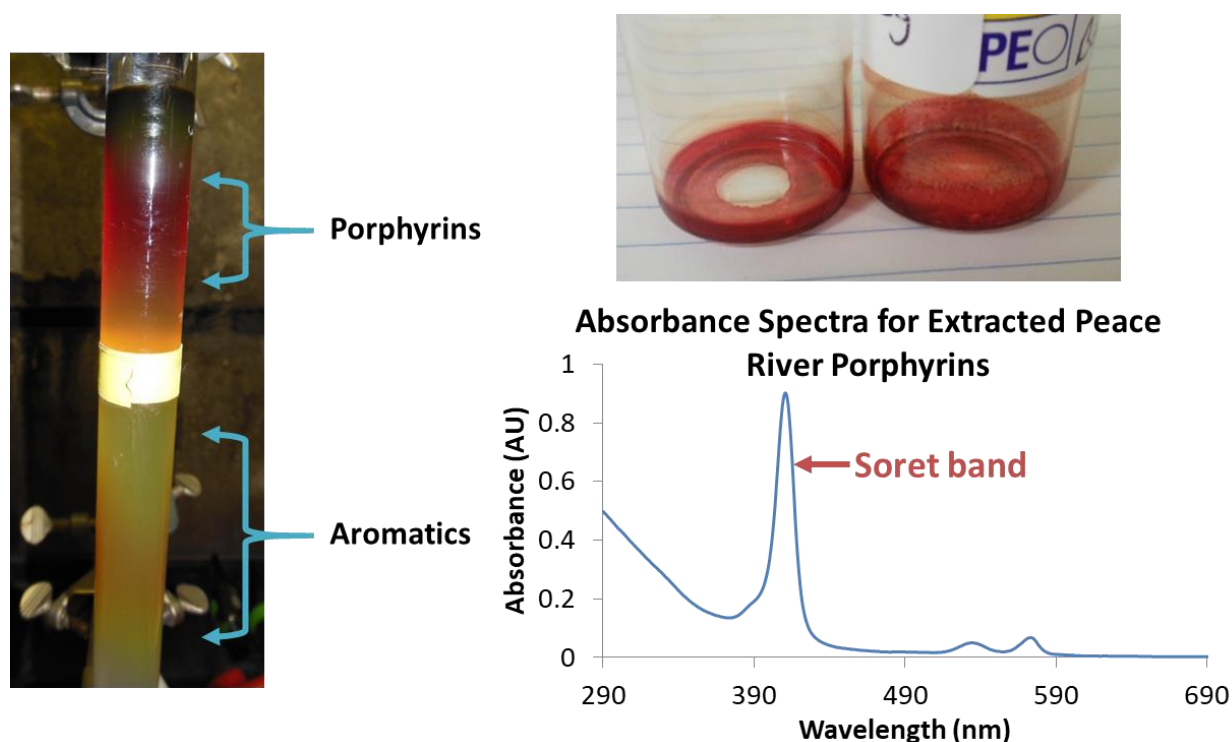


Figure 2. Porphyrins were extracted from Peace River bitumen using column chromatography (**left**), which was dried to give a red-colored porphyrin fraction (**upper right**). This material was analyzed by UV-Visible spectroscopy, which shows the presence of a strong Soret band at 410 nm, confirming the presence of porphyrins. Bands above 500 nm are associated porphyrin Q bands.

For this work, a modification of the CII (MCII) was used because it takes into consideration that the most soluble CyC₆ asphaltenes may be removed from the numerator and placed in the denominator along with the dispersing phase. This is justified because the CyC₆ asphaltenes are consumed during pyrolysis at a similar rate as the Resins fraction, and their association with the free solvent volume indicates that they may be treated separately from the asphaltene nanoaggregate phase. A Maltenes Index (MI) can be calculated to estimate the solvent power of the maltenes phase by omitting the asphaltenes from the CII. Equations for the Coking Index, CII, MCII, and MI are given in Equations (1)–(4):

$$\text{Coking Index} = \frac{\text{CyC}_6}{\text{CH}_2\text{Cl}_2} \quad (1)$$

where:

CyC₆—Cyclohexane asphaltenes;

CH₂Cl₂—Dichloromethane asphaltenes.

$$\text{CII} = \frac{(\text{Sat} + \text{Aro 1} + \text{Total Asphaltenes})}{(\text{Aro 2} + \text{Aro 3} + \text{Resins})} \quad (2)$$

where:

CII—colloidal instability index;

Sat—saturated;

Aro-1, Aro-2, and Aro-3—Aromatic fractions 1, 2, and 3.

$$\text{MCII} = \frac{(\text{Sat} + \text{Aro 1} + \text{Toluene} + \text{CH}_2\text{Cl}_2)}{(\text{Aro 2} + \text{Aro 3} + \text{Resins} + \text{CyC}_6)} \quad (3)$$

where:

MCII—Modified colloidal instability index.

$$MI = \frac{(\text{Sat} + \text{Aro 1})}{(\text{Aro 2} + \text{Aro 3} + \text{Resins})} \quad (4)$$

where:

MI—Maltenes Index.

Changes in SAR-AD fractions as a function of non-catalytic thermal cracking severity were determined by pyrolyzing heavy oil in sealed tubing reactors. Heavy oil (25 g) was loaded into 52 mL capacity Swagelok tubing reactors assembled from 1" stainless steel pipe and 1" VCR weld glands, caps, and gaskets. Reactors were charged with heavy oil (Canadian from Lloydminster or Peace River) and purged with nitrogen. Reactors were sealed and placed in a preheated fluidized sand bath at 400 °C. Pyrolysis was performed under autogenous pressure. Reactors were submerged in the sand bath for a predetermined time and then removed and placed in front of a fan to air cool the reactors so that they were at ambient temperature within 15 min.

Longer reaction times for pyrolysis reactions using FCC slurry oil were performed in a 100 mL high-temperature, high-pressure Series 4590 Micro Reactor system from Parr Instruments Company. The reactor was charged with oil and purged with nitrogen by cycling three times with 300 psi of nitrogen. After the final purge, the reactor was filled with 300 psi of nitrogen. The oil was heated to 430 °C with maximum stirring under autogenous pressure for various residence times. The reaction was cooled to ambient temperature, and the pressure was released. The contents were vacuum distilled to an atmospheric cut point of 240 °C.

A pseudo-delayed coker reaction was performed using a custom 1" stainless steel tubing reactor assembled with Swagelok fittings. The apparatus used a heated nitrogen purge flowing from the bottom of the vertical reactor through a backpressure regulator set to 15 psi, an ambient temperature knockout trap, and finally through two cold traps. The first cold trap was maintained at 0 °C using an ice water bath, and the second trap was maintained at −90 °C using a dry ice/toluene slurry. Lloydminster C₇ asphaltenes (20 g) were placed in the reactor, which was flushed with nitrogen and maintained with a nitrogen flow of 50 mL/min. The reactor was placed in a preheated fluidized sand bath set to 500 °C for 120 min. The coke yield was 45 wt.%, the amount of condensable liquids was 41 wt.%, and the gas was 14 wt.%.

3. Results

3.1. SAR-AD Model Compound Study

To add a chemical meaning to some of the observed processing or behavior phenomena, it is useful to know what kinds of molecules report to the various SAR-AD fractions and obtain some information on the boundaries for those fractions.

From the SAR-AD ELSD chromatogram shown in Figure 1, the first peak (Saturates) is material that ultimately elutes unadsorbed through the silica gel stationary phase with n-heptane as the mobile phase. This material has the weakest interaction with the highly active silica sorbent. This is consistent with saturated hydrocarbons and traditional SARA-type separations. This fraction contains saturated hydrocarbons such as the model compound n-C₂₂, polywax, and natural waxes from crude oils isolated using MEK at −34 °C. For saturated hydrocarbon model compounds, two extremes in structure are abundant in natural hydrocarbons: linear n-alkanes and highly cyclic alkanes. Highly cyclic alkanes are also known as naphthenes or naphthenic hydrocarbons. The elution of highly cyclic alkanes within the saturates fraction was verified by using 5- α -cholestane (Figure 3) as a model compound.

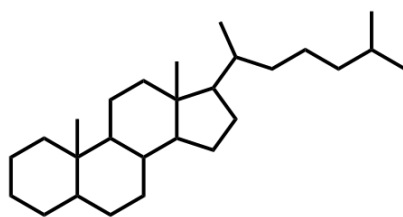


Figure 3. Molecular structure of 5- α -cholestane which reports to the Saturates fraction. Stereochemistry is omitted for clarity.

Shortly after the elution of the Saturates fraction, a second fraction elutes. In most cases, this fraction is not completely chromatographically baseline-resolved from the Saturates fraction. These two closely eluting sets of molecule types are similar except that the material that elutes in the second peak has a stronger interaction with the silica sorbent in the presence of heptane. The enhanced interaction is attributed to the presence of a single aromatic ring, which was confirmed by setting the diode array detector to 180 nm and observing that the Saturates fraction showed no adsorption at this wavelength but that the second peak had a high concentration of molecules that indeed showed absorbance at this wavelength. Using dodecylbenzene (Figure 4) as the model compound, single-ring aromatic compound elution was verified in the second SAR-AD peak. Due to the detection of primarily 1-ring aromatics, this second eluting fraction is termed Aro-1.

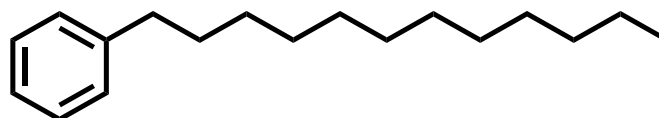


Figure 4. Molecular structure of dodecylbenzene, which reports to the Aro-1 fraction.

In order for single aromatic molecules to be detected in the ELSD, they must be heavily substituted with aliphatic side chains or contain naphthenic structures so that they have a sufficient molecular weight and are not evaporated with the solvent and thus not detected (for example, n-C₂₀ is not detected in the ELSD but n-C₂₂ is detected). This high degree of substitution causes steric hindrance around the aromatic unit, which prevents it from having a high degree of interaction with the silica gel adsorption sites. This is why this fraction is not completely resolved from the Saturates fraction. Evidence for steric hindrance effects on elution is shown later for the model compounds used for the Aro-2 fraction.

To elute the Aro-2 material, which had previously adsorbed onto the highly active silica gel stationary phase using n-heptane, the mobile phase is switched to toluene. From the model compound evaluated, this fraction was found to contain mostly 2 and 3-ring fused aromatic molecules, the pericondensed 4-ring molecule pyrene, and molecules with 3–5 rings that are not fused, such as o-terphenyl; binaphthyl; and 9,10-diphenylanthracene. Figure 5 shows various aromatic molecules that were eluted in the Aro-2 fraction. From the model compounds shown in Figure 5, it is clear that the presence of small pendent alkyl groups (methyl or ethyl) or naphthenic cyclic structuring (1,2,3,6,7,8-hexahdropyrene) does not significantly affect the elution characteristics of these compounds. It should be noted that most of these exact model compounds do not occur at significant levels in unprocessed petroleum. Instead, most petroleum molecules will contain these aromatic core structures that are substituted with various alkyl groups.

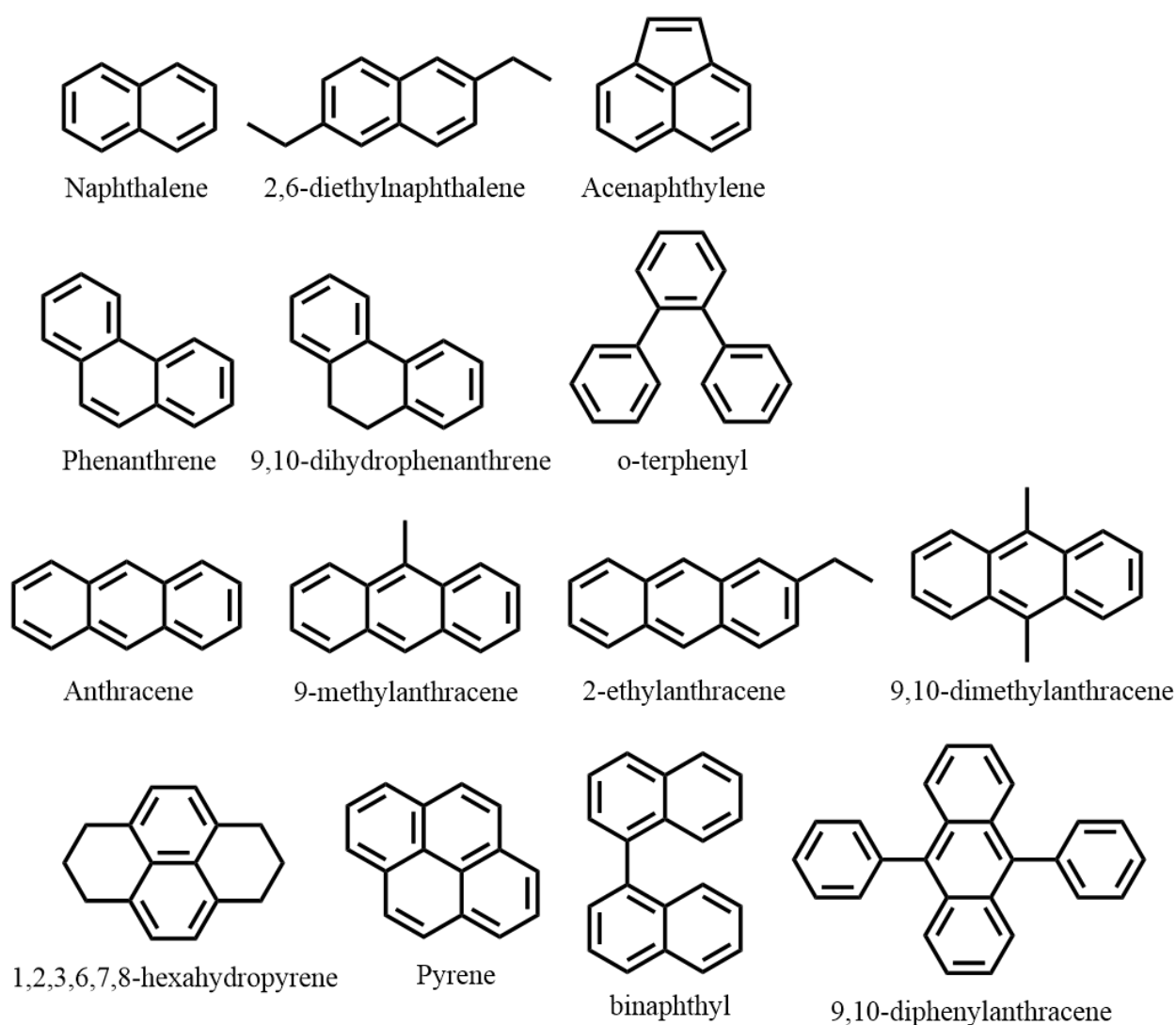


Figure 5. Aromatic model compound molecules that elute in the Aro-2 fraction.

To probe the effect of steric hindrance on elution behavior, naphthalene molecules substituted with alkyl groups of varying steric sizes were analyzed by the SAR-AD. Increasing steric hindrance around the aromatic π -electrons is expected to reduce their interaction with the silica gel sorbent. The model compounds chosen for this study had steric hindrance increasing in the following order: naphthalene; 2,9-diethylnaphthalene; 2,9-diisopropylnaphthalene; and 2,9-ditertbutylnaphthalene (Tolman cone angle for: ethyl = 132° , isopropyl = 160° , and t-butyl = 182° [53]). SAR-AD analysis of these compounds showed that the addition of two ethyl groups provided slight steric bulk to repel the naphthalene core from the sorbent surface, so that about 94% of the compound eluted in Aro-2 (with 6% eluting in Aro-1). The addition of two isopropyl groups significantly altered the elution of the parent naphthalene compound, so that approximately 75% eluted with the Aro-2 fraction. Increasing the steric bulk further by adding the tertbutyl groups slightly affected the elution relative to the isopropyl groups, with 72% eluting with Aro-2. Due to the lack of readily available higher substituted naphthalene compounds, it was not possible to determine the effect of additional isopropyl and tertbutyl groups on the elution behavior of the naphthalene core, but with this limited set of molecules, the trend of steric bulk effects in Aro-1/Aro-2 distribution is evident. Figure 6 shows the molecular structure of the naphthalene model compounds and a visualization of the steric bulk due to the various 2,9-alkyl substituents.

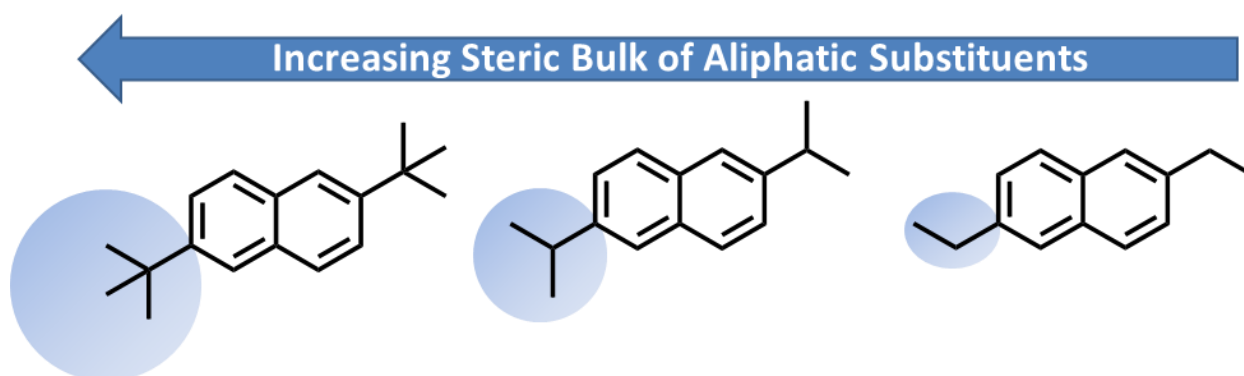


Figure 6. Molecular structures of naphthalene and naphthalene with various 2,9-alkyl substituents and increasing steric bulk. Illustrative steric volumes of pendent alkyl groups are shown in a shaded area. Shaded areas are not to scale. Tolman cone angles are: ethyl = 132° , isopropyl = 160° , and t-butyl = 182° [59].

In common SARA separations, a small number of heteroatoms also begin to appear in the aromatic fraction. Therefore, it was of interest to determine which types of heteroatom functional groups may elute in the Aro-2 fraction. It is not expected that highly polar functional groups such as esters, phenols, carboxylic, thiol, or amines would appear in the aromatics fraction. However, depending on the structure, steric bulk, and electron distributions, less polar groups such as esters and thioethers (or sulfides) may be expected. Figure 7 shows model compounds containing low-polarity oxygen, sulfur, and nitrogen groups that were also found to elute in the Aro-2 fraction.

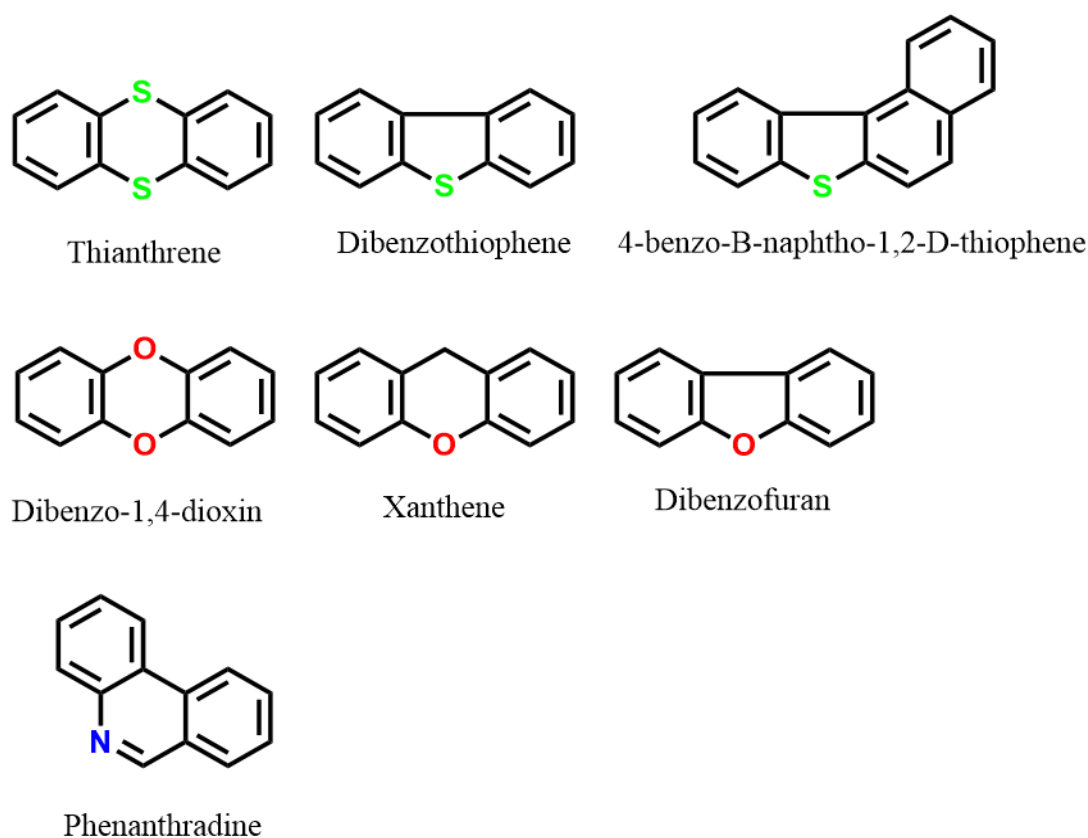


Figure 7. Heteroatoms containing three- and four-ring model compounds that eluted in the Aro-2 fraction. (The green color indicates sulfur atoms, red color oxygen atoms and blue color nitrogen).

After elution of the Aro-2 material, a significant amount of material remains adsorbed on the glass beads and aminopropyl silica columns used in the separation. These two chromatography columns, working in tandem, are the stationary phases used for the elution of the Aro-3 and Resins fractions. Some molecules in the Aro-3 fraction absorb light at 500 nm, indicating a small concentration of molecules with larger aromatic chromophores and/or potentially the presence of low-polarity (sulfide, ether, thiophene, pyrrole, and carbazole) heteroatoms. For the non-heteroatom-containing aromatic molecules where all the rings are fused, the 4-membered linear and catacondensed aromatic model compounds elute with this fraction, as do large polycyclic aromatic hydrocarbons (PAHs) like coronene (with seven fused rings). Substitution of some of these PAHs by one or two methyl groups did not affect the elution relative to the parent PAH core. Figure 8 shows the molecular structure of molecules that eluted with the Aro-3 fraction.

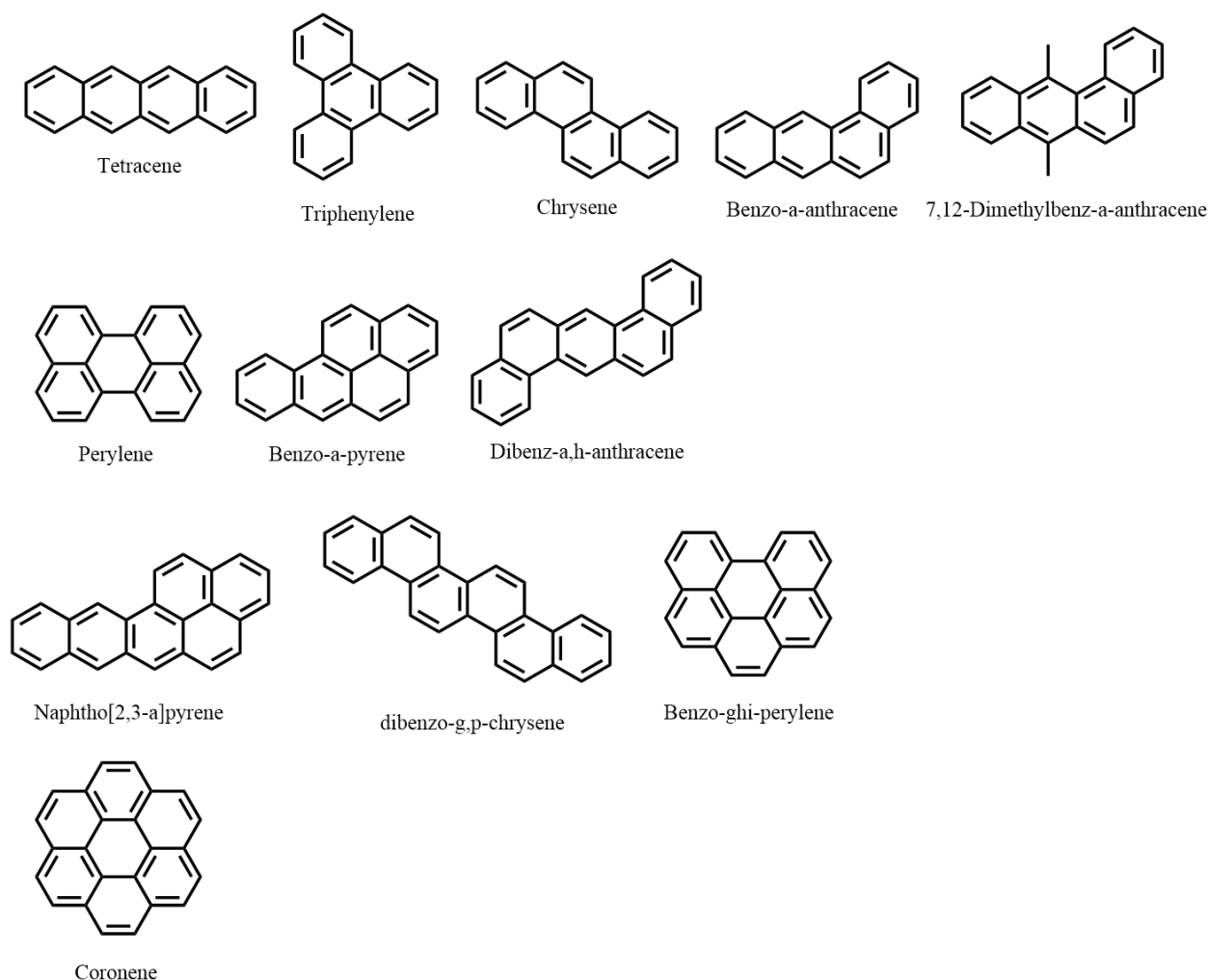


Figure 8. Fused-ring aromatic molecules that eluted to the Aro-3 fraction.

From the model compounds that eluted in the Aro-2 fractions, there were some compounds with additional carbon-carbon bonds (Figure 5) between phenyl or other fused ring units ($C_{ar}-C_{ar}$) that did not alter the elution characteristics of the largest fused ring subunits (9,10-diphenylanthracene and binaphthyl, respectively). It is expected that the addition of additional phenyl groups to other larger fused ring systems would impact the chromatographic cut point between Aro-2 and Aro-3. It was of interest to probe this further since recent work on scanning tunneling microscopy coupled with atomic force microscopy (STM-AFM) has shown that archipelago types of aromatic structures are present in asphaltenes [60]. The archipelago type of asphaltenes identified by STM-AFM do not show

aromatic groups linked by alkyl groups, which was often depicted for archipelago asphaltene structures in early work. Rather, AFM studies generally show direct $C_{ar}-C_{ar}$ bonds linking different aromatic groups to represent archipelago-type molecules. Model compounds analyzed by the non-contact AFM (nc-AFM) method show that aromatic groups connected by long aliphatic linkers are readily detectable and stable with respect to the method, so if they are present in significant amounts they should be readily detected [61]. It should be noted that outside of FCC pitch pyrolysis products [61], to date there has not been evidence for asphaltenes containing significant aliphatic linkages between different aromatic groups, which is why most of the selected model compounds in this work contain aromatic molecules with pendant phenyl or other fused ring groups. For the SAR-AD separation, adding phenyl groups to anthracene did not change its elution from Aro-2, but joining two anthracene molecules together or adding naphthalene to anthracene did increase its interaction with the sorbents, causing it to elute in the Aro-3 fraction. Additionally, large aromatic molecules such as 9,9',10,10'-tetraphenyl-2,2'-bianthracene (MW = 658.84 Daltons), which has a molecular weight similar to asphaltenes, elute exclusively in the Aro-3 fraction. From the non-heteroatom containing aromatic molecules used in this study, no size limit from readily available model compounds was reached, which caused the molecule to elute to more polar fractions, even when using the dye molecule DPB, which has a molecular weight of 804.97 Daltons. However, this does not preclude that other larger, less-soluble, non-heteroatom-containing aromatics, with distinctly different geometries or other combinations of alkyl and aryl substitutions, would prevent these from reporting to the Resins or Asphaltene fractions. It should be noted that substantially larger non-heteroatom aromatics have been identified in asphaltene fractions by nc-AFM55. Figure 9 shows the archipelago-type of model aromatics that eluted with the Aro 3 fraction.

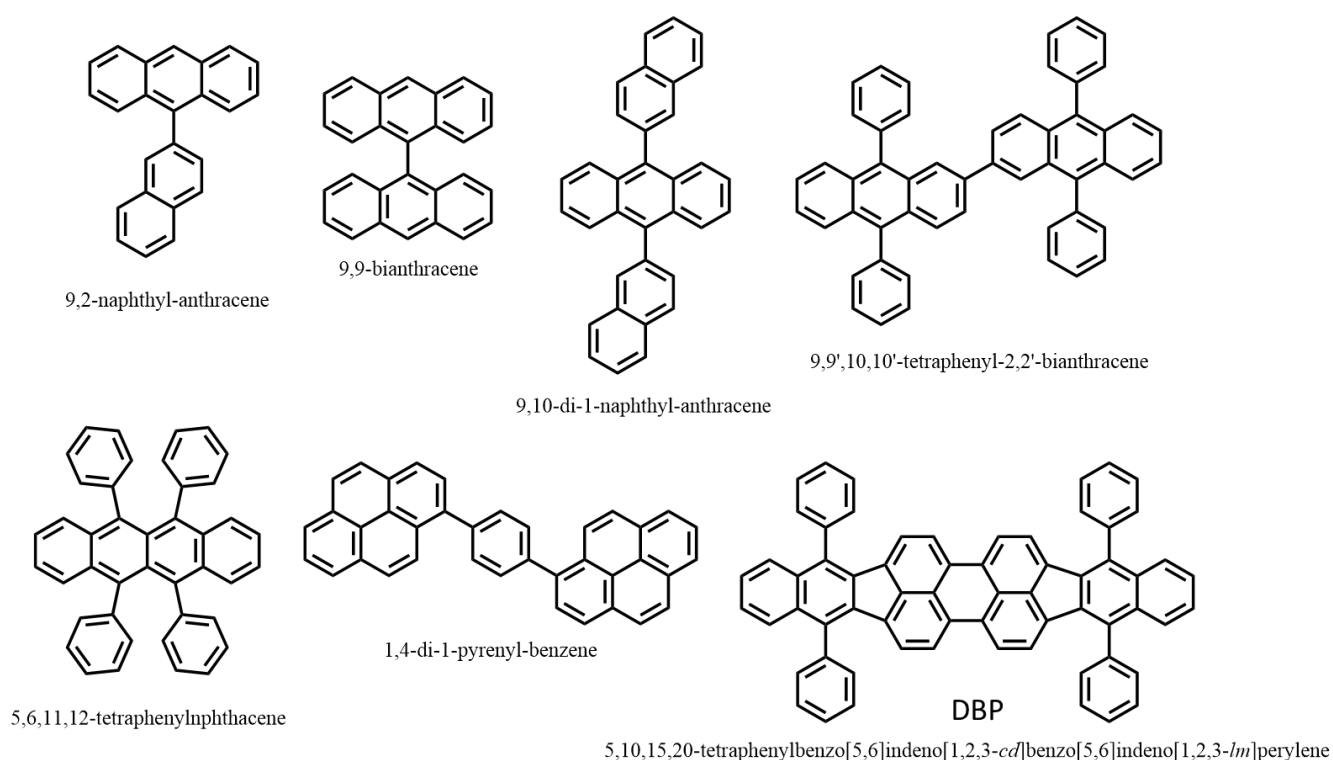
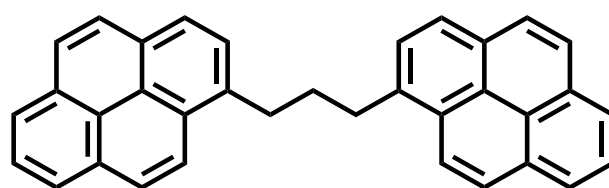


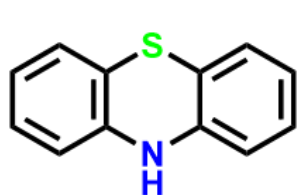
Figure 9. The non-heteroatom contains aromatic molecules, which report to Aro-3 and contain bridging $C_{ar}-C_{ar}$ linkages, with the smaller aromatic cores consisting of three fused aromatic rings (**top row**) and those with four or more fused aromatic rings (**bottom row**).

As mentioned, nc-AFM work on petroleum pitch (M-50, produced through thermal conversion of FCC decant oil to form larger aromatic units for mesophase production and carbon materials) has shown evidence of a minor fraction of molecules with aliphatic carbon-carbon bonds ($C_{al}-C_{al}$) groups joining aromatic units [62,63]. To study the effect of aliphatic linkages between aromatic units, a model compound with two pyrene groups linked together by a propyl group was analyzed by the SAR-AD. This molecule was shown to elute in the Aro-3 fraction (Figure 10), whereas the single aromatic units that are not linked show up in the Aro-2 fraction. The addition of moderately polar functional groups to small aromatic systems, such as pyrrolic, thiazine, or non-aromatic ring ether, can also cause these molecules to report to the Aro-3 fraction. Figure 11 shows model compounds that eluted in the Aro-3 fraction that would have otherwise eluted in the Aro-2 fraction without their functional groups (it was ambiguous for indene if it would have eluted in the Aro-1 or Aro-2 fraction because it was not able to be detected by ELSD or by absorbance at 290 nm).

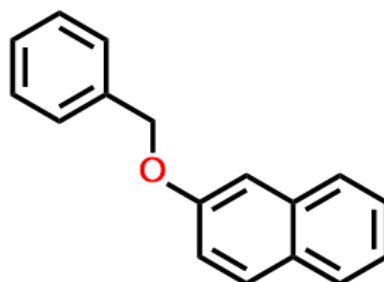


1,3-Di-(1-pyrenyl)propane

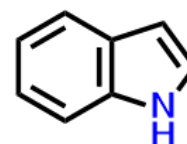
Figure 10. Aromatic molecules with bridging $C_{al}-C_{al}$ linkages 1,3-di-(1pyrenyl) propane, which is linked by an aliphatic propyl group. This molecule eluted in the Aro-3 fraction.



Phenothiazine



Benzyl-2-naphthyl ether



Indole

Figure 11. Examples of aromatic molecules that eluted to the Aro-3 fraction that would have otherwise eluted in the Aro-2 fraction if the heteroatoms were replaced by carbon atoms. (The green color designates sulfur atom, the blue color—NH group, and the red color—oxygen atom).

Other functional groups, like carbazole, can cause non-heteroatom parent PAHs that report to Aro-3 to partially elute into the subsequent Resins fraction. For example, tetracene elutes exclusively with the Aro-3 fraction. However, by replacing the aromatic unit with a pyrrolic group, such as in 11H-benzo[a]carbazole, the molecule begins to partition into the Resins fraction (15%). By adding another aromatic unit and also changing the geometry of the molecule from a linear to a “U” shape (7H-dibenzo[c,g] carbazole), a greater net dipole is present, and the pyrrolic molecule contributes even more in the Resins fraction (30%). Figure 12 shows the molecular structures for 11H-benzo[a]carbazole and 7H-dibenzo[c,g] carbazole. In general, the slight shift to the Resins fraction due to the pyrrolic functional groups is not as significant as for other functional groups.

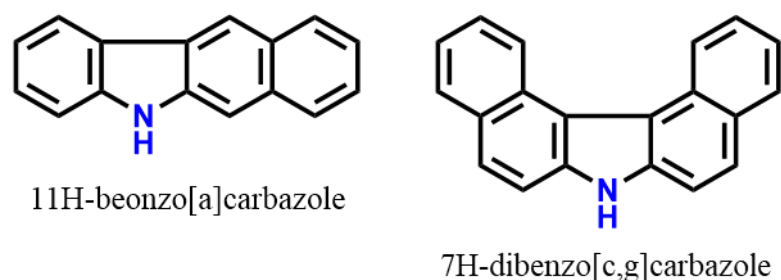


Figure 12. Molecular structures for pyrrolics containing 11H-benzo[a]carbazole and 7H-dibenzo[c,g]carbazole. These molecules belong mostly to the Aro-3 fraction and partially to the Resins fraction. (The blue color indicates the NH group).

More polar ketone and acyl groups connected to Aro-2 parent molecules (like anthracene or pyrene) cause these molecules to report heavily to the Aro-3 fraction with only minor partitioning into the Resins fraction ($\sim <10\%$). Similar elution patterns were observed with the addition of the amino group in 1-aminopyrene. However, this observation may be more related to the interaction of the amine functional groups with the aminopropyl silica sorbent. Figure 13 shows some examples of model molecules that report mostly to the Aro-3 fraction but would otherwise report to the Aro-2 fraction in the absence of the functional groups.

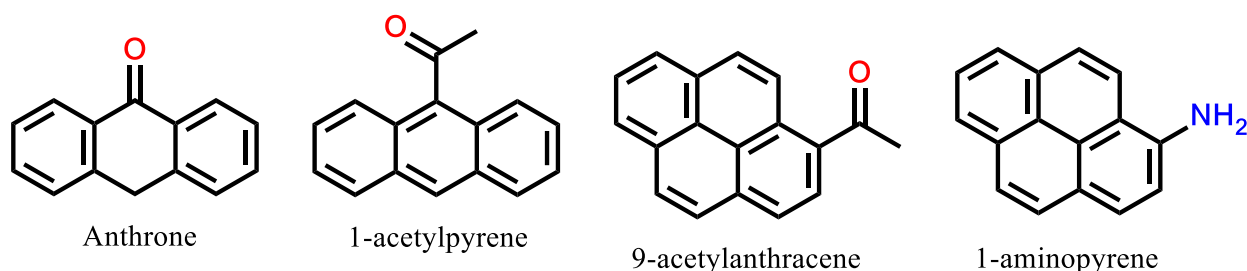


Figure 13. Examples of aromatic molecules that eluted to the Aro-3 fraction that would have otherwise eluted in the Aro-2 fraction if the heteroatoms were replaced by hydrogen atoms. (The red color indicates oxygen atom, and the blue color—the NH_2 group).

Hydroxyl groups are significantly more polar than ketone and acyl groups, and they can participate in strong intermolecular hydrogen-bonding interactions. By placing a hydroxyl group on a highly saturated hydrocarbon, it causes the molecule to report to the Aro-3 fraction with some elution into the Resins fraction (about 10%). This is the case with beta-sitosterol (Figure 14).

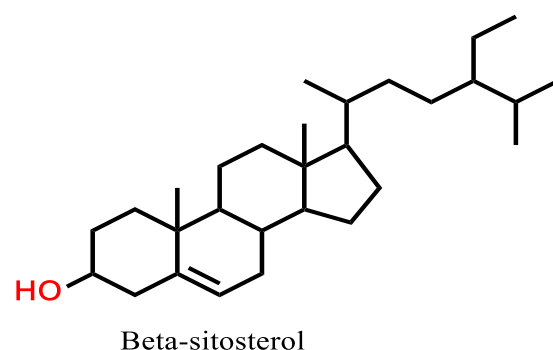


Figure 14. The molecular structure of beta-sitosterol has been attributed mainly to the Aro-3 fraction ($\sim 90\%$) due to the presence of the hydroxyl group. Stereochemistry is omitted for clarity. (The red color indicates OH group).

Phenolic groups are more acidic than aliphatic hydroxyl groups and are expected to produce stronger intermolecular hydrogen bonding. In 4-nonylphenol and 4-dodecylphenol, the phenolic groups and aromatic rings cause these molecules to report exclusively to the Resins fraction. Without the phenolic OH groups, these molecules would normally report to the Aro-1 fraction. Likewise, phenolic groups on anthracene and pyrene cause these molecules to report to the Resins fraction, whereas without the phenolic groups, the parent fused-ring aromatic molecules would report to the Aro-2 fraction. The addition of a less acidic methanolic ($\text{CH}_2\text{-OH}$) functional group on fused-ring aromatics, such as 9-anthracenemethanol, also caused the compound to report to the Resins fraction. Other polar functional groups can significantly change the elution of Aro-2 parent fused-ring molecules to report to the Resins fraction. For instance, having two pyridinic nitrogen atoms, as in 1,10'-phenanthroline, allows for a strong chelating effect of the nitrogen groups at active sorbent sites, also causing this molecule to report to the Resins fraction. It is likely that nitrogen substitution at other positions may not have such a strong effect since they would not lend themselves to the chelating effect; for instance, the single nitrogen in phenanthradine still caused the molecule to report to the Aro-2 fraction (Figure 7), like its non-nitrogen-containing analogue phenanthrene. Figure 15 shows various model compound molecules that eluted in the Resins fraction that would otherwise report to less polar aromatic fractions in the absence of their heteroatoms.

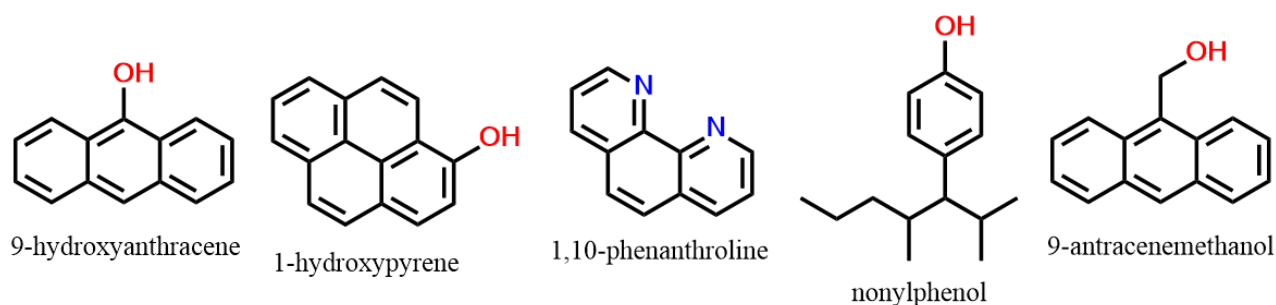
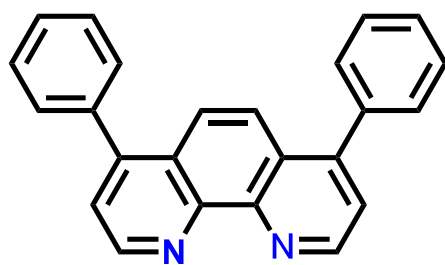


Figure 15. Molecular structures of model compounds that eluted to the Resins fraction. For simplicity, a single isomeric structure for nonylphenol is shown. (The red color indicates OH group, while the blue color designates nitrogen atom).

As shown in Figure 1 and as mentioned previously, elution of asphaltenes occurs in SAR-AD after Aro-1, but will be discussed at this time to preserve continuity of the bitumen solubility/polarity spectrum discussion. Finding reasonable model compounds that report to the three SAR-AD asphaltene subfractions is not trivial. Interestingly, addition of phenyl groups to 1,10-phenanthroline, as is the case with bathophenanthroline (Figure 16), caused this compound to elute between the Toluene asphaltenes and the Resins fraction. The split between the two fractions was around 1:1. It should be noted that the SAR-AD separation was not optimized to separate discrete pure compounds but rather to provide a generic and highly repeatable cut point for the separation of complex mixtures of thousands of different compounds. Therefore, it is expected that some model compounds will not cleanly report to a single fraction.

Other types of molecules that were found to report to the asphaltene subfractions were acenaphthenequinone; Coumarin 343; acenaphthenequinone; N,N-bis-2-ethylhexyl-3,4,9,10-perylenetetracarboxylic diimide; and the charged Reichardt's dye molecule. Admittedly, these molecules are not ideal asphaltene models in terms of covering asphaltene average properties for molecular weight, heteroatom content, aromaticity, and functional group type. However, they do provide some insight about the SAR-AD separation and the relationship between molecular size, structure, and functional groups. The molecular structures of the asphaltene model compounds are shown in Figure 17.



Bathophenanthroline

Figure 16. Molecular structure for bathophenanthroline, which reports to the Resins and Toluene asphaltene fraction (1:1).

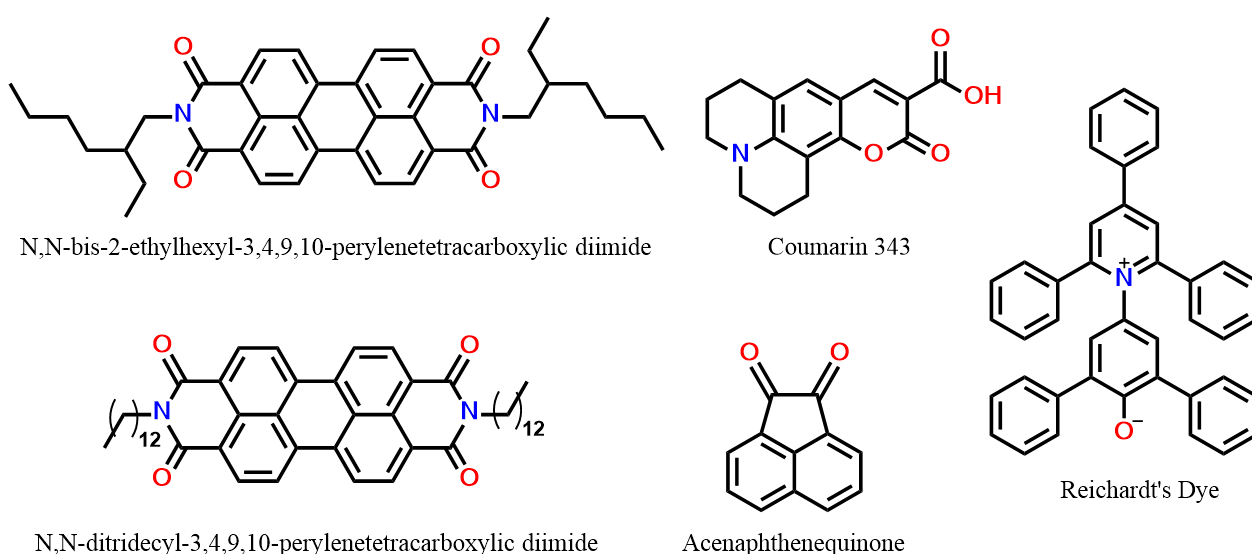


Figure 17. Molecular structure for model compounds acenaphthenequinone (MW = 182.17 Daltons); Coumarin 343 (MW = 285.29 Daltons); N,N-bis-2-ethylhexyl-3,4,9,10-perylenetetracarboxylic diimide (MW = 614.79 Daltons); and N,N-ditridecyl-3,4,9,10-perylenetetracarboxylic diimide (MW = 755.06 Daltons). Reichardt's dye reports to the CH₂Cl₂ asphaltenes, while the other molecules elute to the Toluene asphaltenes.

With the exception of Reichardt's dye, all of these molecules consist of polar carbonyl groups, and Coumarin 343 also consists of a carboxylic group. For model compounds to be insoluble in heptane (and thus precipitated on the first analytical column using the SAR-AD technique) but soluble in toluene, there needs to be a balance between the size, polarity (such as the very small but polar acenaphthenequinone), and aromaticity. Coumarin 343 is small and contains a polar carbonyl and carboxylic group, but has two naphthenic cycles, and N,N-bis-2-ethylhexyl-3,4,9,10-perylenetetracarboxylic diimide (MW = 614.79 Daltons) contains four carbonyl groups but two longer branched aliphatic chains. It should be noted that the longer-chain compound N,N-ditridecyl-3,4,9,10-perylenetetracarboxylic diimide (MW = 755.06 Daltons) was also tested and eluted mostly in the Toluene asphaltene fraction, but it was significantly less soluble. Again, with the exception of Reichardt's dye, other asphaltene model compounds showed up primarily in the Toluene asphaltenes, with less than 10% reporting to the CH₂Cl₂ asphaltenes. On the other hand, Reichardt's dye, a charged molecule, reported primarily to the CH₂Cl₂ asphaltene fraction. It would be of interest to determine more realistic model compounds that report to the three different asphaltene subfractions, especially the CyC₆ asphaltenes and CH₂Cl₂ asphaltenes, since these fractions are heavily impacted by the oxidation of asphalt and the pyrolysis of various petroleum feedstocks (the Coking Index for example). It is also important to determine

if blends of the various compounds cause interactions that change their co-solubility or elution behavior.

A limited study was performed using porphyrins and their metal complexes. Metalloporphyrins are extremely important since they affect catalyst performance and coke quality. For more aliphatic porphyrins, like octaethylporphyrin, and more aromatic tetraphenylporphyrin, both of these molecules were reported to the Aro-3 fraction. These results are consistent with those of other model compounds in this study, which showed that the pyrrolic group is not highly polar. The metalation of nickel II to etioporphyrin is not expected to change the polarity of the porphyrin system significantly. This was confirmed as the etioporphyrin I nickel complex reported to the Aro-3 fraction. Figure 18 shows the molecular structures for octaethylporphyrin, tetraphenylporphyrin, and etioporphyrin I nickel.

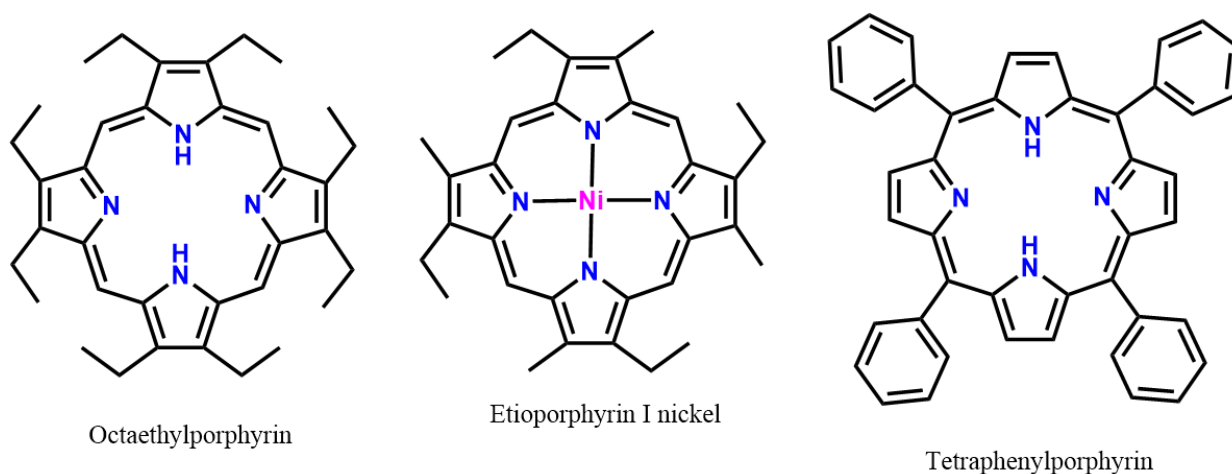


Figure 18. Molecular structures for octaethylporphyrin, tetraphenylporphyrin, and etioporphyrin I nickel, which elute the Aro-3 fraction.

However, vanadium IV oxide porphyrins contain an out-of-plane carbonyl group, which would induce a strong dipole in the complex, causing it to become more polar. This was confirmed as vanadyl octaethylporphyrin eluting in the Resins fraction. Figure 19 shows the molecular structure of vanadyl octaethylporphyrin.

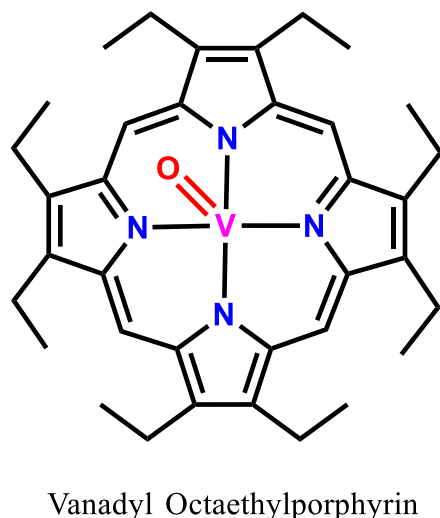


Figure 19. Molecular structure for vanadyl octaethylporphyrin, which elutes to the Resins fraction.

For validation, the petroleum porphyrins concentrated from the Canadian Peace River bitumen (Figure 2) were analyzed by SAR-AD and were found to be concentrated primarily in the Aro-3 and Resins fractions (1.2:1 by ELSD), with less than 10% also showing up in the asphaltenes.

3.2. SAR-AD Hydrocracker Relationships

The primary issue that needs to be overcome with ebullated bed vacuum residues is the formation of coke-like sediments that deposit on the reactor and downstream vessels as well as on the catalyst surface and cause both operability and rapid catalyst deactivation problems [64,65]. Their level in the hydrocracked residual oils determines the hydrocracking reaction severity [66], and it is considered acceptable when the total sediment existent (TSE) in the atmospheric tower bottom (ATB) product is no higher than 0.3–0.4 wt.%. Such a level of ATB TSE guarantees smooth operation and achievement of the planned cycle length between two consecutive cleanings of the commercial ebullated bed vacuum residue hydrocracker unit. In this research, nine cases were investigated where the vacuum residue conversion varied between 55 and 91%. For these cases, the SAR-AD fraction contents, along with reaction temperature, liquid hourly space velocity (LHSV), and bulk properties of the hydrocracked vacuum residues, called vacuum tower bottoms (VTBs), are presented in Table 2.

The data in Table 2 show that the ATB sediment content for the studied cases varied between 0.04 and 2.2 wt.%. Three of the ATB TSE cases are distinguishable because their sediment is greater than 0.4 wt.%. These are higher than the allowable limits, and, as a result, they caused increased fouling in the commercial hydrocracker [54,67].

In order to assess which parameters contribute to the increased ATB sediment content, an intercriteria analysis (ICrA) of the data in Table 2 was performed. The ICrA evaluation determines the degrees of correlation between the criteria, depending on the user's choice of μ and ν . These correlations between the criteria are classified as follows: 'positive consonance', 'negative consonance' or 'dissonance' [68]. The values of μ in the range $0.75 \div 1.00$ and $\nu = 0.00 \div 0.25$ denote a statistically meaningful positive relation. Respectively, the values of negative consonance with $\mu = 0.00 \div 0.25$ and $\nu = 0.75 \div 1.0$ represent a statistically meaningful negative relation. Details of the ICrA application to investigate petroleum property relations are given in our prior publications [61,62].

To visualize the results in the ICrA evaluation for index matrices M^μ and M^ν , we use color scales, which can be achieved with a simple function as the "Conditional Formatting" in Excel, e.g., from green for the results equal to complete intuitionistic fuzzy truth, i.e., the pair $\langle 1,0 \rangle$ to red for the results equal to complete intuitionistic falsity, i.e., the pair $\langle 0,1 \rangle$. This colorization scheme allows for more immediate visual detection and interpretation of the results. Two software packages for ICrA have been developed and are freely available as open source from <https://intercriteria.net/software/> (accessed on 21 March 2023); they are described in further detail in [69–72]. Tables 3 and 4 summarize the results for μ and ν values of the ICrA evaluation.

Table 2. Bulk properties and SAR-AD characteristics of hydrocracked vacuum residues (VTB) obtained at the commercial LNB H-Oil hydrocracker.

Cases	Case 1	Case 2	Case 3	Case 4	Case 5	Case 6	Case 7	Case 8	Case 9
Date	22 December 2015	6 November 2015	10 July 2017	21 January 2019	9 May 2017	16 April 2019	12 August 2020	21 February 2022	11 April 2022
Crude slate	100% Urals	100% Urals	85% Ur/ 15% ME	80% Ur./ 20% ME	70% Ur./ 30% ME	14% Ur. 36% LSCO /50% ME	61.5% Ur/ 3% BL/ 2% AM/ 19.5% Kirkuk /7.5% LSCO /6.5% Prinos	64% Ur /25% Kirkuk /11% BL	88.6% Ur/ 5% LSCO/6.5% Kirkuk
FCC slurry, % in H-Oil feed	0.0	0.0	7.6	6.1	8.2	7.5	13.1	0.0	11.5
H-Oil VTB recycle, % of feed	0.0	0.0	0.0	0.0	0.0	0.0	29.4	0.0	0.0
Weight average bed temperature. °C	409	418	426	425	428	426	430.5	429.5	414.5
LHSV. h-1	0.23	0.25	0.21	0.20	0.20	0.17	0.10	0.16	0.14
Atmospheric tower bottom product (ATB) SHFT. wt. %	0.3	2.2	0.4	0.4	0.25	0.04	0.11	0.55	0.46
H-Oil 540 °C + conversion. wt. %	55	65	71.6	73	74.5	76.3	90.8	78	62
Density at 15 °C. g/cm ³	0.985	1.005	1.029	1.033	1.041	1.034	1.093	1.066	1.018
Conradson carbon. wt. %	17.9	20.4	24.4	26	25.5	25.8	35.0	30.5	14.9
Sulfur. wt. %	1.1	1.3	1.38	1.24	1.4	1.3	1.3	1.9	1.3
SAR-AD characteristics									
Saturates, wt. %	27.44	26.98	21.01	21.96	19.76	19.72	13.85	18.66	21.48
Aro-1, wt. %	9.34	8.22	6.85	7.15	6.77	7.48	3.04	5.92	8.41
Aro-2, wt. %	18.76	17.43	16.89	17.82	17.35	18.80	14.75	18.07	20.30
Aro-3, wt. %	33.41	34.59	43.04	40.77	44.09	44.86	60.20	44.74	39.67
Resins, wt. %	6.03	5.93	5.97	6.19	6.01	4.37	2.46	4.42	4.17
CyC ₆ asphaltenes, wt. %	0.38	0.34	0.23	0.25	0.23	0.17	0.07	0.22	0.14
Toluene asphaltenes, wt. %	4.47	6.12	5.56	5.47	5.47	4.28	4.90	7.00	5.28
CH ₂ Cl ₂ asphaltenes, wt. %	0.18	0.39	0.46	0.39	0.33	0.32	0.71	0.95	0.53
Total asphaltenes, wt. %	5.03	6.85	6.24	6.11	6.03	4.77	5.68	8.17	5.95
CyC ₆ /CH ₂ Cl ₂	2.10	0.89	0.49	0.66	0.71	0.55	0.10	0.23	0.27
TPA	16.96	17.96	18.96	19.96	19.96	20.96	11.22	14.24	10.71
Colloidal instability index (CII)	0.718	0.726	0.517	0.544	0.483	0.470	0.292	0.487	0.559
Maltenes Index (MI)	0.632	0.607	0.423	0.449	0.393	0.400	0.218	0.365	0.466
Modified colloidal instability index (MCII)	0.707	0.715	0.512	0.538	0.478	0.466	0.290	0.482	0.555

Table 3. μ -value of the ICRA evaluation of relations between bulk properties, SAR-AD characteristics of H-Oil VTB, and reaction severity. SLO = FCC slurry (% in H-Oil feed), Rec = H-Oil VTB recycle (% of feed), TRX = Weight average bed temperature ($^{\circ}\text{C}$), LHSV = LHSV (h^{-1}), ATB TSE = Atmospheric tower bottom product (ATB) SHFT (wt.%), Conv. = H-Oil 540 $^{\circ}\text{C}$ + conversion (wt.%), D15 = Density at 15 $^{\circ}\text{C}$ (g/cm^3), CCR = Conradson carbon (wt.%), Sul = Sulfur (wt.%).

MU	SLO	Rec	TRX	LHSV	ATB TSE	Conv.	D15	CCR	Sul	Sat	Aro-1	Aro-2	Aro-3	Resins	CyC ₆	Toluene	CH ₂ Cl ₂	Total	CyC ₆ /CH ₂ Cl ₂	TPA	CII	MI	MCII
SLO	1.00	0.31	0.61	0.19	0.28	0.56	0.61	0.47	0.44	0.28	0.31	0.36	0.64	0.28	0.14	0.28	0.58	0.28	0.22	0.42	0.25	0.28	0.25
Rec	0.31	1.00	0.25	0.03	0.06	0.22	0.22	0.22	0.14	0.00	0.00	0.00	0.22	0.00	0.03	0.08	0.22	0.06	0.00	0.06	0.00	0.00	0.00
TRX	0.61	0.25	1.00	0.25	0.36	0.92	0.92	0.83	0.67	0.08	0.03	0.28	0.89	0.36	0.22	0.56	0.64	0.56	0.22	0.50	0.14	0.03	0.14
LHSV	0.19	0.03	0.25	1.00	0.58	0.19	0.19	0.25	0.31	0.81	0.67	0.42	0.22	0.75	0.86	0.64	0.28	0.61	0.83	0.61	0.75	0.75	0.75
ATB TSE	0.28	0.06	0.36	0.58	1.00	0.33	0.33	0.36	0.47	0.64	0.56	0.53	0.28	0.53	0.58	0.78	0.64	0.81	0.47	0.33	0.75	0.64	0.75
Conv.	0.56	0.22	0.92	0.19	0.33	1.00	0.94	0.92	0.61	0.08	0.11	0.36	0.92	0.36	0.22	0.50	0.58	0.50	0.25	0.58	0.14	0.08	0.14
D15	0.61	0.22	0.92	0.19	0.33	0.94	1.00	0.86	0.64	0.08	0.11	0.36	0.92	0.36	0.22	0.50	0.64	0.50	0.25	0.53	0.14	0.03	0.14
CCR	0.47	0.22	0.83	0.25	0.36	0.92	0.86	1.00	0.53	0.17	0.14	0.33	0.83	0.44	0.31	0.50	0.61	0.53	0.28	0.58	0.22	0.17	0.22
Sul	0.44	0.14	0.67	0.31	0.47	0.61	0.64	0.53	1.00	0.17	0.17	0.33	0.61	0.36	0.28	0.61	0.58	0.61	0.25	0.42	0.28	0.17	0.28
Sat	0.28	0.00	0.08	0.81	0.64	0.08	0.08	0.17	0.17	1.00	0.86	0.61	0.06	0.72	0.83	0.50	0.31	0.53	0.83	0.47	0.89	0.94	0.89
Aro-1	0.31	0.00	0.03	0.67	0.56	0.11	0.11	0.14	0.17	0.86	1.00	0.75	0.14	0.58	0.69	0.36	0.28	0.39	0.75	0.50	0.81	0.92	0.81
Aro-2	0.36	0.00	0.28	0.42	0.53	0.36	0.36	0.33	0.33	0.61	0.75	1.00	0.39	0.44	0.47	0.39	0.39	0.42	0.56	0.47	0.61	0.67	0.61
Aro-3	0.64	0.22	0.89	0.22	0.28	0.92	0.92	0.83	0.61	0.06	0.14	0.39	1.00	0.28	0.14	0.47	0.61	0.47	0.22	0.56	0.06	0.06	0.06
Resins	0.28	0.00	0.36	0.75	0.53	0.36	0.36	0.44	0.36	0.72	0.58	0.44	0.28	1.00	0.86	0.50	0.28	0.53	0.78	0.69	0.67	0.67	0.67
CyC ₆	0.14	0.03	0.22	0.86	0.58	0.22	0.22	0.31	0.28	0.83	0.69	0.47	0.14	0.86	1.00	0.56	0.25	0.58	0.86	0.56	0.78	0.78	0.78
Toluene	0.28	0.08	0.56	0.64	0.78	0.50	0.50	0.50	0.61	0.50	0.36	0.39	0.47	0.50	0.56	1.00	0.64	0.97	0.47	0.42	0.56	0.44	0.56
CH ₂ Cl ₂	0.58	0.22	0.64	0.28	0.64	0.58	0.64	0.61	0.58	0.31	0.28	0.39	0.61	0.28	0.25	0.64	1.00	0.67	0.14	0.25	0.42	0.31	0.42
Total	0.28	0.06	0.56	0.61	0.81	0.50	0.50	0.53	0.61	0.53	0.39	0.42	0.47	0.53	0.58	0.97	0.67	1.00	0.47	0.39	0.58	0.47	0.58
CyC ₆ /CH ₂ Cl ₂	0.22	0.00	0.22	0.83	0.47	0.25	0.25	0.28	0.25	0.83	0.75	0.56	0.22	0.78	0.86	0.47	0.14	0.47	1.00	0.61	0.72	0.78	0.72
TPA	0.42	0.06	0.50	0.61	0.33	0.58	0.53	0.58	0.42	0.47	0.50	0.47	0.56	0.69	0.56	0.42	0.25	0.39	0.61	1.00	0.42	0.47	0.42
CII	0.25	0.00	0.14	0.75	0.75	0.14	0.14	0.22	0.28	0.89	0.81	0.61	0.06	0.67	0.78	0.56	0.42	0.58	0.72	0.42	1.00	0.89	1.00
MI	0.28	0.00	0.03	0.75	0.64	0.08	0.03	0.17	0.17	0.94	0.92	0.67	0.06	0.67	0.78	0.44	0.31	0.47	0.78	0.47	0.89	1.00	0.89
MCII	0.25	0.00	0.14	0.75	0.75	0.14	0.14	0.22	0.28	0.89	0.81	0.61	0.06	0.67	0.78	0.56	0.42	0.58	0.72	0.42	1.00	0.89	1.00

Note: Green color denotes statistically meaningful positive relation; red color denotes statistically meaningful negative relation. The intensity of the color designates the strength of the relation. The higher the color intensity, the higher the strength of the relation. Yellow color denotes dissonance.

Table 4. ν -value of the ICRA evaluation of relations between bulk properties, SAR-AD characteristics of H-Oil VTB, and reaction severity. SLO = FCC slurry (% in H-Oil feed), Rec = H-Oil VTB recycle (% of feed), TRX = Weight average bed temperature ($^{\circ}\text{C}$), LHSV = LHSV (h^{-1}), ATB TSE = Atmospheric tower bottom product (ATB) SHFT (wt.%), Conv. = H-Oil 540 $^{\circ}\text{C}$ + conversion (wt.%), D15 = Density at 15 $^{\circ}\text{C}$ (g/cm^3), CCR = Conradson carbon (wt.%), Sul = Sulfur (wt.%).

Nu	SLO	Rec	TRX	LHSV	ATB TSE	Conv.	D15	CCR	Sul	Sat	Aro-1	Aro-2	Aro-3	Resins	CyC ₆	Toluene	CH ₂ Cl ₂	Total	CyC ₆ /CH ₂ Cl ₂	TPA	CII	MI	MCII
SLO	0.00	0.00	0.28	0.69	0.61	0.36	0.31	0.44	0.31	0.64	0.61	0.56	0.28	0.64	0.75	0.61	0.31	0.64	0.69	0.47	0.67	0.64	0.67
Rec	0.00	0.00	0.00	0.22	0.19	0.00	0.00	0.00	0.08	0.22	0.22	0.22	0.00	0.22	0.22	0.17	0.03	0.17	0.22	0.19	0.22	0.22	0.22
TRX	0.28	0.00	0.00	0.69	0.58	0.06	0.06	0.14	0.14	0.89	0.94	0.69	0.08	0.61	0.72	0.39	0.31	0.42	0.75	0.44	0.83	0.94	0.83
LHSV	0.69	0.22	0.69	0.00	0.36	0.78	0.78	0.72	0.50	0.17	0.31	0.56	0.75	0.22	0.08	0.36	0.67	0.36	0.14	0.39	0.22	0.22	0.22
ATB TSE	0.61	0.19	0.58	0.36	0.00	0.64	0.64	0.61	0.33	0.33	0.42	0.44	0.69	0.44	0.36	0.17	0.31	0.17	0.50	0.61	0.22	0.33	0.22
Conv.	0.36	0.00	0.06	0.78	0.64	0.00	0.06	0.08	0.22	0.92	0.89	0.64	0.08	0.64	0.75	0.47	0.39	0.50	0.75	0.39	0.86	0.92	0.86
D15	0.31	0.00	0.06	0.78	0.64	0.06	0.00	0.14	0.19	0.92	0.89	0.64	0.08	0.64	0.75	0.47	0.33	0.50	0.75	0.44	0.86	0.97	0.86
CCR	0.44	0.00	0.14	0.72	0.61	0.08	0.14	0.00	0.31	0.83	0.86	0.67	0.17	0.56	0.67	0.47	0.36	0.47	0.72	0.39	0.78	0.83	0.78
Sul	0.31	0.08	0.14	0.50	0.33	0.22	0.19	0.31	0.00	0.67	0.67	0.50	0.22	0.47	0.53	0.19	0.22	0.22	0.58	0.39	0.56	0.67	0.56
Sat	0.64	0.22	0.89	0.17	0.33	0.92	0.92	0.83	0.67	0.00	0.14	0.39	0.94	0.28	0.14	0.47	0.67	0.47	0.17	0.50	0.11	0.06	0.11
Aro-1	0.61	0.22	0.94	0.31	0.42	0.89	0.89	0.86	0.67	0.14	0.00	0.25	0.86	0.42	0.28	0.61	0.69	0.61	0.25	0.47	0.19	0.08	0.19
Aro-2	0.56	0.22	0.69	0.56	0.44	0.64	0.64	0.67	0.50	0.39	0.25	0.00	0.61	0.56	0.50	0.58	0.58	0.58	0.44	0.50	0.39	0.33	0.39
Aro-3	0.28	0.00	0.08	0.75	0.69	0.08	0.08	0.17	0.22	0.94	0.86	0.61	0.00	0.72	0.83	0.50	0.36	0.53	0.78	0.42	0.94	0.94	0.94
Resins	0.64	0.22	0.61	0.22	0.44	0.64	0.64	0.56	0.47	0.28	0.42	0.56	0.72	0.00	0.11	0.47	0.69	0.47	0.22	0.28	0.33	0.33	0.33
CyC ₆	0.75	0.22	0.72	0.08	0.36	0.75	0.75	0.67	0.53	0.14	0.28	0.50	0.83	0.11	0.00	0.39	0.69	0.39	0.11	0.39	0.19	0.19	0.19
Toluene	0.61	0.17	0.39	0.36	0.17	0.47	0.47	0.47	0.19	0.47	0.61	0.58	0.50	0.47	0.39	0.00	0.31	0.00	0.50	0.58	0.42	0.53	0.42
CH ₂ Cl ₂	0.31	0.03	0.31	0.67	0.31	0.39	0.33	0.36	0.22	0.67	0.69	0.58	0.36	0.69	0.69	0.31	0.00	0.31	0.83	0.69	0.56	0.67	0.56
Total	0.64	0.17	0.42	0.36	0.17	0.50	0.50	0.47	0.22	0.47	0.61	0.58	0.53	0.47	0.39	0.00	0.31	0.00	0.53	0.58	0.42	0.53	0.42
CyC ₆ /CH ₂ Cl ₂	0.69	0.22	0.75	0.14	0.50	0.75	0.75	0.72	0.58	0.17	0.25	0.44	0.78	0.22	0.11	0.50	0.83	0.53	0.00	0.36	0.28	0.22	0.28
TPA	0.47	0.19	0.44	0.39	0.61	0.39	0.44	0.39	0.39	0.50	0.47	0.50	0.42	0.28	0.39	0.58	0.69	0.58	0.36	0.00	0.56	0.50	0.56
CII	0.67	0.22	0.83	0.22	0.22	0.86	0.86	0.78	0.56	0.11	0.19	0.39	0.94	0.33	0.19	0.42	0.56	0.42	0.28	0.56	0.00	0.11	0.00
MI	0.64	0.22	0.94	0.22	0.33	0.92	0.97	0.83	0.67	0.06	0.08	0.33	0.94	0.33	0.19	0.53	0.67	0.53	0.22	0.50	0.11	0.00	0.11
MCII	0.67	0.22	0.83	0.22	0.22	0.86	0.86	0.78	0.56	0.11	0.19	0.39	0.94	0.33	0.19	0.42	0.56	0.42	0.28	0.56	0.00	0.11	0.00

Note: Green color denotes statistically meaningful positive relation; red color denotes statistically meaningful negative relation. The intensity of the color designates the strength of the relation. The higher the color intensity, the higher the strength of the relation. Yellow color denotes dissonance.

Based on the μ and ν values of the ICRA evaluation, one can see that the sediment content in the H-Oil ATB product has statistically meaningful positive relationships with the total asphaltene content ($\mu = 0.81$; $\nu = 0.17$); the Toluene asphaltenes ($\mu = 0.78$; $\nu = 0.17$); the CII ($\mu = 0.75$; $\nu = 0.22$); and the MCII ($\mu = 0.75$; $\nu = 0.22$). These results confirm that asphaltenes are primarily responsible for sediment formation during hydrocracking due to their inclination to aggregate, strongly adsorb to surfaces, and promote condensation and crosslinking reactions [73–87]. The data in Tables 3 and 4 suggest that the concentration of Toluene asphaltenes, which are the predominant part of the H-Oil VTB, affects the sediment formation in the H-Oil hydrocracked residual oils. The results also show that CH_2Cl_2 asphaltenes have a stronger influence on the sediment content than C_6 asphaltenes. However, the most polar pre-coked CH_2Cl_2 asphaltenes at these low levels in the feeds may not be as polar as the Toluene asphaltenes because they are almost an order of magnitude smaller in amount.

Apart from asphaltene content, sediment formation has been reported to be significantly affected by reaction conditions like LHSV, reaction time, temperature, pressure, and catalytic active site concentration [76,77,80–82,87]. This can explain why the positive consonance of the H-Oil ATB sediment content with the VTB asphaltene content alone, although statistically meaningful, is still weak. This implies that the LHSV, the fresh catalyst addition rate (solid catalyst and liquid nano-dispersed HCAT [53,67] catalyst), and the temperature (pressure is constant) applied at the commercial ebullated bed vacuum residue hydrocracker also have a significant impact on the sediment formation rate.

The data in Tables 3 and 4 indicate that the reaction temperature has strong statistically meaningful consonances with conversion (positive; $\mu = 0.92$; $\nu = 0.06$), Saturate content (negative; $\mu = 0.08$; $\nu = 0.89$), Aro-1 content (negative; $\mu = 0.03$; $\nu = 0.94$), Maltene Index (negative; $\mu = 0.03$; $\nu = 0.94$) and intermediate consonances with Aro-3 content (positive; $\mu = 0.89$; $\nu = 0.08$), and the colloidal instability index (negative; $\mu = 0.14$; $\nu = 0.83$). These findings show that the increase in reaction temperature understandably enhances the conversion of the thermally sensitive Saturates, and Aro-1, with some dependence on Aro-3 components. With increasing temperature, thermal cracking reactions increase more rapidly than their hydrogen addition counterparts [88]. Increasing temperature results in the rapid depletion of VTB Saturates, and Aro-1. These two fractions can continue thermal cracking and conversion, eventually producing gas. However, polyaromatic core structures mostly remain intact, and if they do not become small enough to enter the vapor phase, they can eventually undergo crosslinking and coke formation.

The relationship between polycyclic aromatic molecules in Aro-3 is complex. Cleavage of aliphatic groups, or smaller pendant aromatics, from Aro-3 polyaromatic cores should mostly result in producing smaller Aro-3 core molecular fragments from the parent molecule.

During hydrocracking, some FCC slurry oil is added to the blends. FCC slurry oil is highly aromatic and enriched in predominantly 3–5 aromatic ring systems [89] and is a good control oil to shed some light on the behavior of the aromatic fractions during pyrolysis. Pyrolysis experiments with FCC slurry oil showed that Aro-3 increased due to aromatic addition reactions. This is shown in Table 5. Coincidentally, this experiment also shows the rapid degradation and near-complete conversion of the Saturates fraction, consistent with alkane pyrolysis. In addition to these factors, Aro-3 molecules can be produced by the thermal degradation of asphaltenes. For asphaltenes, both island- and archipelago-type structures have been identified in a wide range of crude sources at varying ratios, which also has a significant impact on various fluid and processing phenomena [90–94]. The amount of Aro-3 produced will be highly dependent on the chemistry of the asphaltenes and whether they are more island- or archipelago-type. In a hydrocracker, hydrogen is intended to cap radicals produced from thermal bond breaking, so it is likely that aromatic addition reactions are somewhat retarded, as in the case of aromatic growth occurring in the FCC slurry oil. In the case of the production of Aro-3 from asphaltenes, this is likely more favored in the presence of hydrogen, as further reactions of heavy molecules

and Aro-3 molecular fractions to form coke will be depressed. However, hydrogen is not expected to influence the initial amount of parent Aro-3 molecules fragmenting into cracked Aro-3 molecules. These results suggest that Aro-3 has a distinct and dominant reactivity, especially when compared to Aro-2. Prevailing Aro-3 relationships are likely because the reactivity of this fraction will have a large impact since it is the most abundant of the maltene fractions for the oils surveyed here. The special reaction sensitivity of this fraction may be inferred from oxidation experiments, which show that the Aro-3 fraction is readily consumed in air at 100 °C under a pressure of 2.1 mPa [95]. It is well known that benzyl carbons on aromatic molecules are some of the most reactive compounds in bitumen, so it is reasonable that they are easily reacted during pyrolysis and hydrocracking [96,97].

Table 5. SAR-AD data for FCC slurry oil pyrolyzed at 430 °C at different retention times.

Hours	Saturates	Aro-1	Aro-2	Aro-3	Resins	CyC ₆	Toluene	CH ₂ Cl ₂	Total Asp.
0	17.47	0.00	46.19	34.94	0.73	0.00	0.65	0.02	0.67
2	6.63	0.00	40.25	46.68	1.12	0.00	4.56	0.76	5.32
2.5	0.52	0.00	29.10	57.22	0.86	0.00	9.91	2.39	12.30

The LHSV has weak statistically meaningful consonances with conversion (negative; $\mu = 0.19$; $\nu = 0.78$), Saturate content (positive; $\mu = 0.81$; $\nu = 0.17$), Aro-3 content (negative; $\mu = 0.22$; $\nu = 0.75$), Resin content (positive; $\mu = 0.75$; $\nu = 0.22$), CyC₆ asphaltene content (positive; $\mu = 0.86$; $\nu = 0.08$), CII, and Maltene Index (positive; $\mu = 0.75$; $\nu = 0.22$). These findings are in line with expectations, as they show that the increase in LHSV (decrease in reaction time) leads to decreased conversion due to a low level of thermal cracking in the ebullated bed vacuum residue hydrocracking [98,99]. The level of cracking with increased LHSV will be more similar to early thermal cracking since there is less time for interaction with the catalyst and hydrogen. From this analysis, the Saturates content has a strong positive relationship with LHSV, which is likely due to its thermal sensitivity. The decomposition of Saturates relative to Aro-2 and Aro-3 is easily seen in Table 5 for FCC slurry oil, but it is not as easily seen when pyrolyzing heavy oil, as seen in Table 6 and Figure 20. This is because in the case of heavy oil, a significant amount of saturates are also generated from all the other aromatic, resin, and asphaltene fractions while the original Saturates fraction is being cracked (Table 7 shows Saturates generated from pyrolysis of only the asphaltenes). Resins and CyC₆ asphaltenes also have a positive consonance, which is related to their sensitivity to thermal cracking, as shown in Table 6 and Figure 20. It is interesting to note the sensitivity of the Resins and CyC₆ fractions since, if a molecular continuum is assumed, the main difference between these fractions and Aro-3 is largely driven by polar heteroatoms. These heteroatoms may decrease the energy barrier to thermal bond cracking in the aromatic cores, which should be explored in more detail. The Resins and CyC₆ fractions are more soluble than the other asphaltene fractions, which allows them to remain in solution longer and endure a higher level of cracking before phase separation and forming coke.

Table 6. SAR-AD data after 400 °C pyrolysis of Lloydminster vacuum residue at increasing residence time.

min @ 400 °C	Sat	Aro-1	Aro-2	Aro-3	Resins	CyC ₆	Toluene	Cl ₂ Cl ₂	Total Asph.
0	14.0	7.5	8.5	36.7	18.8	4.0	10.3	0.1	14.4
10	15.5	8.2	10.1	35.6	16.8	3.6	10.2	0.1	13.8
20	16.3	8.8	10.2	35.4	15.1	2.2	11.9	0.1	14.2
30	17.4	9.3	10.4	35.1	12.6	1.1	13.9	0.2	15.2
40	17.7	9.9	10.7	35.6	9.2	0.8	15.4	0.8	16.9
50	17.6	9.7	10.3	35.1	9.3	0.6	16.3	1.0	17.9
60	17.3	9.4	10.4	35.9	7.9	0.5	16.1	2.4	19.0

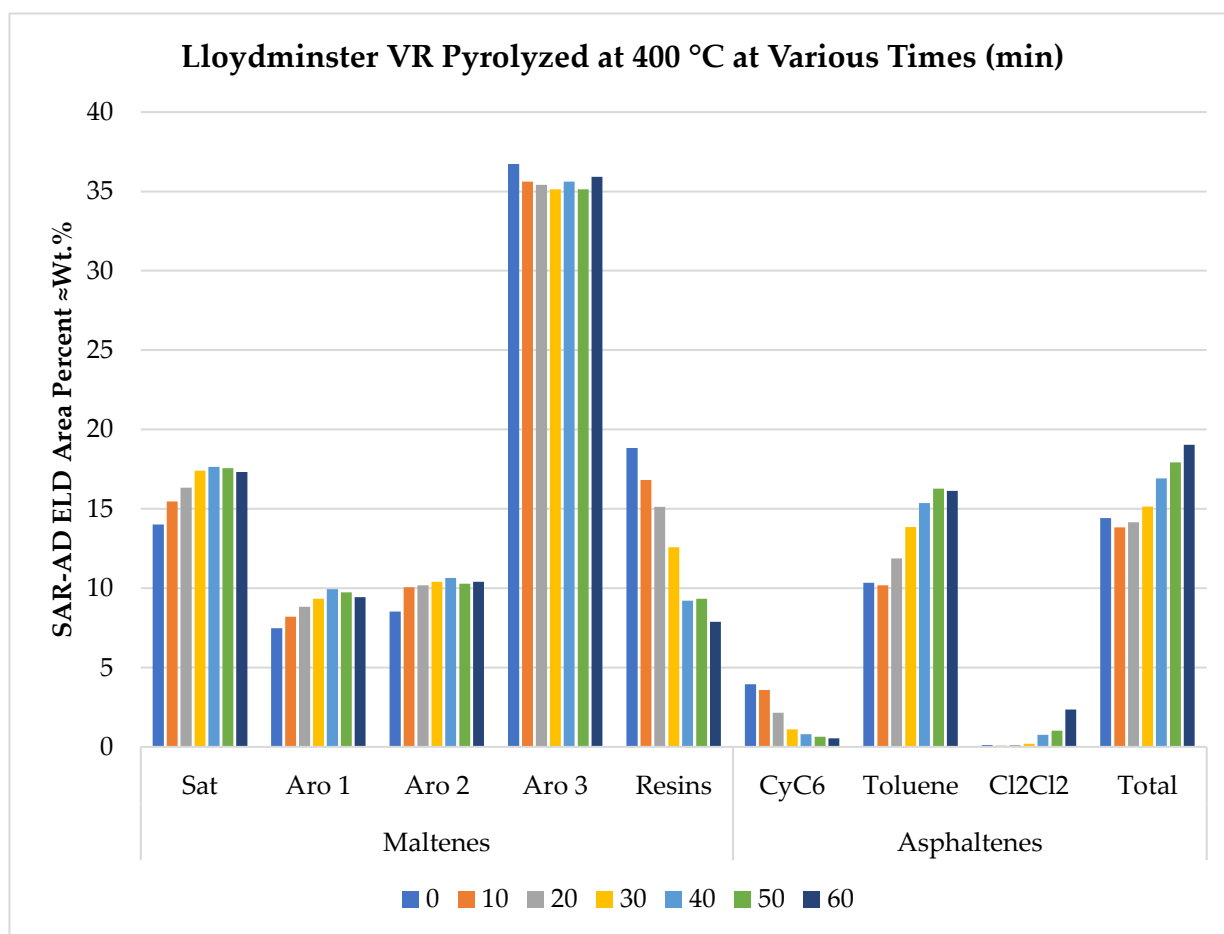


Figure 20. Plot showing the change in SAR-AD fraction from the pyrolysis of Lloydminster vacuum residue in Table 7.

Table 7. SAR-AD data for liquids produced from Lloydminster asphaltenes after heating to 500 °C.

Sample ID	Saturates	Aro-1	Aro-2	Aro-3	Resins	CyC ₆	Toluene	CH ₂ Cl ₂	Total Asp.
Coked Lloydminster Asphaltenes	15.62	9.02	47.13	24.55	1.28	0.11	2.09	0.20	2.40

For the various indices, CII, MCII, and MI, the MI had the strongest consonances with the following characterization factors: density at 15 °C (negative; $\mu = 0.03$; $\nu = 0.97$), conversion (negative; $\mu = 0.08$; $\nu = 0.92$), and CCR (negative; $\mu = 0.17$; $\nu = 0.83$). Whereas the CII and MCII were the same for conversion and density at 15 °C (negative; $\mu = 0.14$; $\nu = 0.86$) and the CCR had a lower consonance (negative; $\mu = 0.22$; $\nu = 0.78$). These relationships are expected since more aliphatic maltenes will result in higher conversion, less density, and lower coke. This is consistent with the results above. However, this does not mean that asphaltenes can be neglected because, for practical applications, they dominate catalyst performance and ATB TSE.

Figures 21 and 22 display plots of variation of Saturates, Aro-1, Aro-2, Aro-3, Resins, CyC₆, Toluene, and CH₂Cl₂ asphaltene fractions in the H-Oil VTBs with conversion severity juxtaposed against these SAR-AD components in the feeds. It is evident from the data in Figure 21 that Saturates increase in the VTB until very high conversion.

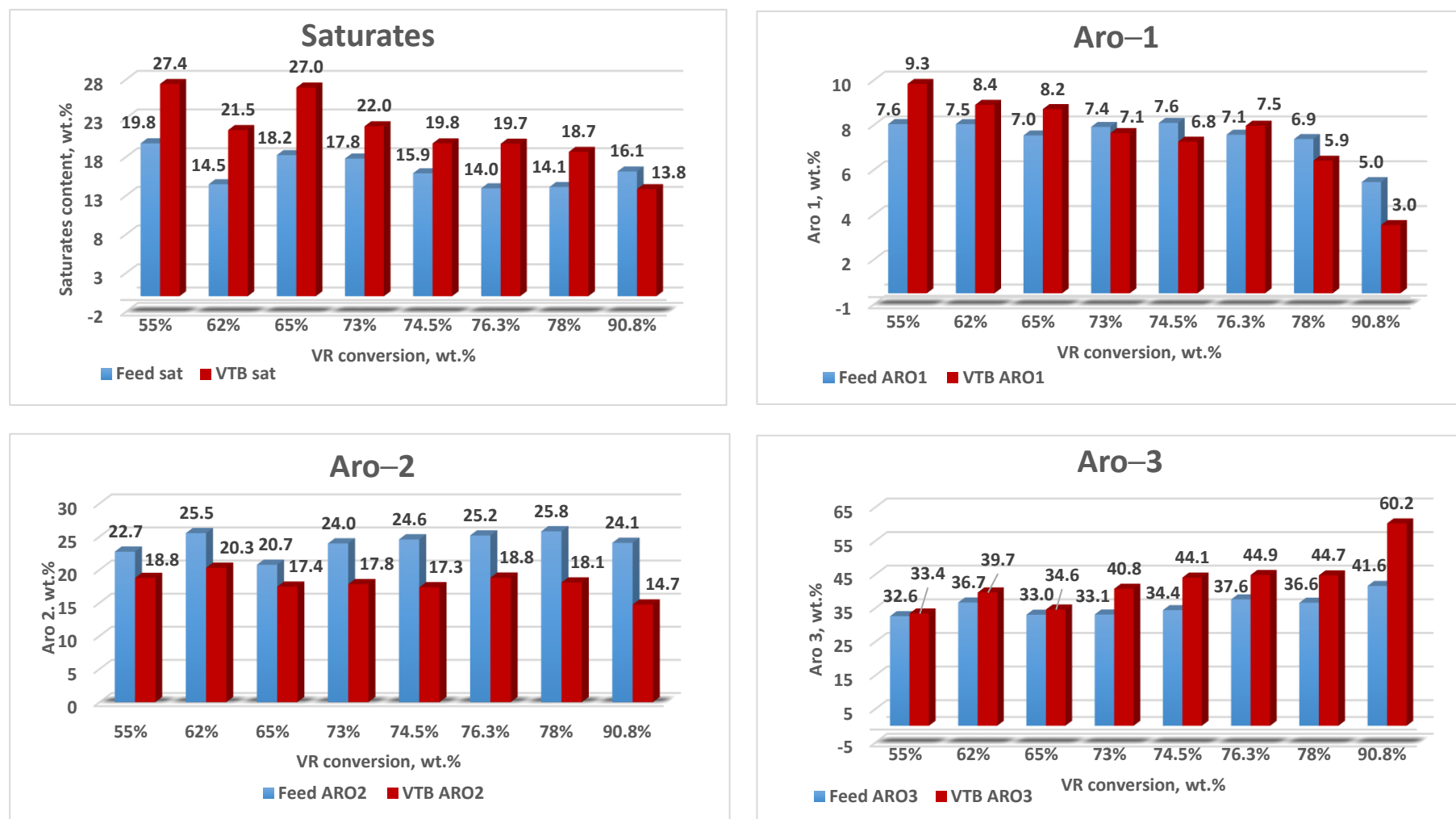


Figure 21. Variation of Saturates, Aro-1, Aro-2, and Aro-3 content in the H-Oil VTBs with conversion alteration, juxtaposed against these SAR-AD components in the feeds.

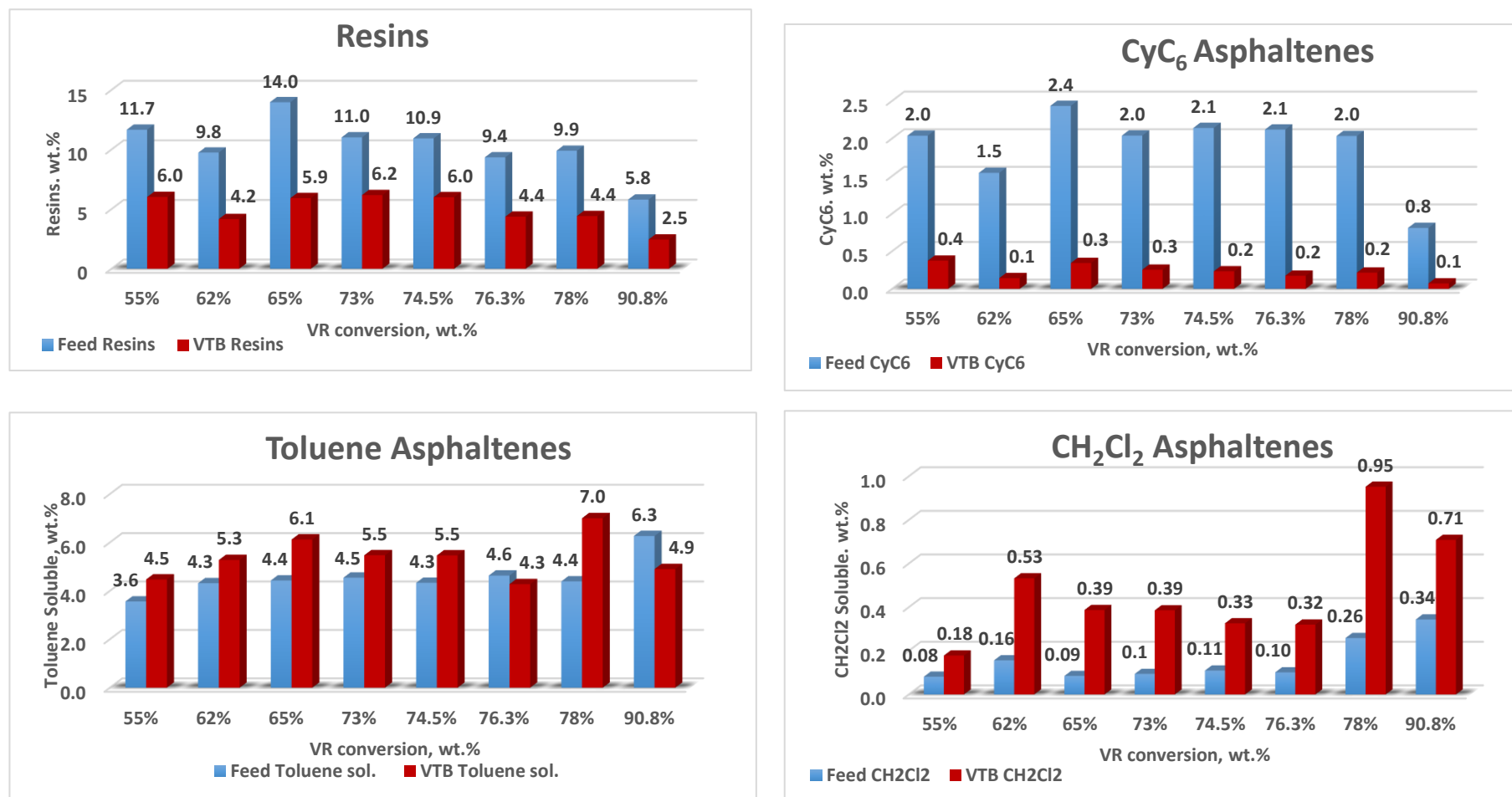


Figure 22. Variation of Resins and CyC₆, Toluene, and CH₂Cl₂ asphaltene content in the H-Oil VTBs with conversion alteration, juxtaposed against these SAR-AD components in the feeds.

This is because aliphatic saturated molecules can be liberated from aromatic cores when cracking asphaltenes and other heavy fractions. This is consistent with observations during thermal cracking without catalyst and hydrogen, as shown in Figure 20. Ultimately, at the highest conversion, the Saturates fraction in the VTB trended lower than the feeds, consistent with further cracking of saturate molecules decreasing in molecular weight with conversion, allowing them to be more easily removed during distillation as lighter fuel fractions. A similar trend was observed for Aro-1, except that the decrease in the VTB with conversion occurred sooner. This is consistent with the fact that Aro-1 is very similar to the Saturates fraction, and this justifies placing the Aro-1 fraction in the numerator for indices such as CII, MCII, and MI.

For the more aromatic fractions—containing fused ring systems—the Aro-2 fraction content initially decreases in the hydrocracked vacuum residue and continues decreasing with amplification of conversion, while that of Aro-3 fraction increases with conversion enhancement. Amounts of Aro-2 decrease because this fraction initially consists of molecules with 2–4 fused rings, and cracking aliphatic groups allows the residual cores to become lighter and more easily distilled. Alternatively, some aromatic ring addition reactions may occur, as in the case of FCC slurry oil (Table 5), to potentially generate Aro-3 and other molecules. Aro-3 molecules have 4+ fused rings, preventing them from becoming significantly volatile, even under severe pyrolysis and complete cracking of pendant groups. Evidence for the production of Aro-3 has also been demonstrated by coking Lloydminster archipelago-type asphaltenes, as previously mentioned (Table 6).

Various models were developed to correlate the SAR-AD data to the ebullated bed VTB hydrocracker conversion level. The dependence of the feed Saturates, Aro-1, Aro-2, and Aro-3 is expressed by the regression Equations (5)–(8). These equations reflect what is observed in the data in Figure 21, indicating that all three fractions—Saturate, Aro-1, and Aro-2—decrease their contents in the hydrocracked vacuum residue, with their contents diminishing in the feed and with enhancement of the conversion. The VTB Aro-3 fraction content also decreases with lower feed Aro-3 content but increases with conversion. As explained, this increase is probably dominated by the breakdown of asphaltene archipelago structures to generate 4+ ring aromatic molecules.

$$\text{VTB}_{\text{Saturates}} = 33.28 + 0.617046 * \text{Feed}_{\text{Saturates}} - 0.30778 * \text{Conversion} \quad (5)$$

$$R = 0.946; \text{Error} = 5.5\%$$

where:

$\text{VTB}_{\text{Saturates}}$ —Saturate content in the vacuum tower bottom (hydrocracked vacuum residue);

$\text{Feed}_{\text{saturates}}$ —Saturate content in the feed.

$$\text{VTB}_{\text{Aro1}} = 10.32 + 0.759841 * \text{Feed}_{\text{Aro1}} - 0.11986 * \text{Conversion} \quad (6)$$

$$R = 0.974; \text{Error} = 4.7\%$$

where:

VTB_{Aro1} —Aro-1 fraction content in the VTB;

$\text{Feed}_{\text{Aro1}}$ —Aro-1 fraction content in the feed.

$$\text{VTB}_{\text{Aro2}} = 13.62 + 0.597046 * \text{Feed}_{\text{Aro2}} - 0.14038 * \text{Conversion} \quad (7)$$

$$R = 0.940; \text{Error} = 2.4\%$$

where:

VTB_{Aro2} —Aro-2 fraction content in the VTB;

$\text{Feed}_{\text{Aro2}}$ —Aro-2 fraction content in the feed.

$$\begin{aligned} \text{VTB}_{\text{Aro3}} &= -32.84 + 1.233803 \cdot \text{Feed}_{\text{Aro3}} + 0.439633 \cdot \text{Conversion} \\ R &= 0.977; \text{Error} = 3.6\% \end{aligned} \quad (8)$$

where:

VTB_{Aro3} —Aro-3 fraction content in the VTB;

$\text{Feed}_{\text{Aro3}}$ —Aro-3 fraction content in the feed.

The data in Figure 22 show that the contents of Resins and CyC_6 asphaltenes in the VTB are lower than those in the feed, while the content of CH_2Cl_2 asphaltenes in the VTB is higher than that in the feed. The amount of the Toluene asphaltene fraction is higher than that in the feed in six of the nine cases studied. The decrease in Resins and CyC_6 asphaltenes with a corresponding increase in CH_2Cl_2 asphaltenes is consistent with previous observations [51] and thermal cracking data for Lloydminster vacuum residue as shown in Table 7 and Figure 20. When this data in Figure 20 is compared to Figure 22, the observed trends between thermal cracking and hydrocracking are quite similar.

With respect to the Toluene asphaltenes, during thermal cracking, the amount generally increases until 50 min, when it begins to decrease with a substantial increase in the CH_2Cl_2 asphaltenes. This suggests that this fraction is an intermediate fraction in that some molecules form Resins and CyC_6 asphaltenes become new Toluene asphaltenes as they lose their solubilizing aliphatic side chains, while at the same time the indigenous Toluene asphaltenes likewise transform to CH_2Cl_2 asphaltenes due to the loss of aliphatic groups. At higher conversion, the new Toluene asphaltenes also convert to CH_2Cl_2 asphaltenes, and with further conversion, they ultimately become coke [51].

The developed regression Equations (9)–(11) show that the contents of Resins, CyC_6 , and CH_2Cl_2 asphaltene fractions in the VTB depend only on the contents of these fractions in the feed.

$$\begin{aligned} \text{VTB}_{\text{Resins}} &= 0.5026 \cdot \text{Feed}_{\text{Resins}} - 0.233 \\ R &= 0.885; \text{Error} = 9.8\% \end{aligned} \quad (9)$$

where:

$\text{VTB}_{\text{resins}}$ —resins content in the VTB;

$\text{Feed}_{\text{resins}}$ —resins content in the feed.

$$\begin{aligned} \text{VTB}_{\text{CyC}_6} &= 0.10872 \cdot \text{Feed}_{\text{CyC}_6} - 0.00401 \\ R &= 0.864; \text{Error} = 18.6\% \end{aligned} \quad (10)$$

where:

$\text{VTB}_{\text{CyC}_6}$ — CyC_6 asphaltene content in the VTB;

$\text{Feed}_{\text{CyC}_6}$ — CyC_6 asphaltene content in the feed.

$$\begin{aligned} \text{VTB}_{\text{CH}_2\text{Cl}_2} &= 3.5294 \cdot \text{Feed}_{\text{CH}_2\text{Cl}_2} \\ R &= 0.960; \text{Error} = 19.4\% \end{aligned} \quad (11)$$

where:

$\text{VTB}_{\text{CH}_2\text{Cl}_2}$ — CH_2Cl_2 asphaltene content in the VTB;

$\text{Feed}_{\text{CH}_2\text{Cl}_2}$ — CH_2Cl_2 asphaltene content in the feed.

In order to explore the effect of the SAR-AD eight-fraction composition of the studied straight-run vacuum residual oils processed in the LNB commercial H-Oil hydrocracker, it was necessary to define the conversion level and the sediment formation rate obtained during processing of the individual vacuum residues. Unfortunately, it is common practice at the refinery to process crude oil blends instead of individual crude oils, with the exception of the Urals crude oil, which is still processed individually. Another feature of the commercial ebullated bed vacuum residue hydrocracking is that it operates at an approximately constant sediment level in the ATB product to guarantee fulfillment of the planned cycle length between two consecutive cleanings. Thus, it is not possible to compare the individual vacuum residue hydrocracking behaviors at different sediment formation rates. Therefore, the behavior of the studied individual vacuum residues was compared

at the same sediment formation rate. Based on our past experience for distinguishing the effects of the different individual feedstocks processed in blends by fluid catalytic cracking and hydrocracking [99], during the adoption of the approximate linear combination technique [100,101], we determined the conversion levels of 22 feeds whose SAR-AD fraction contents were measured (Table 8). After regression of the data for these 22 individual vacuum residues that were processed in the commercial LNB H-Oil hydrocracker, the following Equation (12) was developed.

$$\text{SRVR}_{\text{Conversion}} = 65.04 - 0.5659\text{VR}_{\text{Asp}} - 0.1051\text{VR}_{\text{Res}} + 2.783\text{VR}_{\text{Sul}} \quad (12)$$

$R = 0.983$; Error = 0.78%

where:

$\text{SRVR}_{\text{Conversion}}$ —Conversion of the straight-run vacuum residue;

VR_{Asp} —Asphaltene content in the vacuum residue;

VR_{Res} —Resins content in the vacuum residue;

VR_{Sul} —Sulfur content in the vacuum residue.

It is clear from Equation (12), with plotted regression results in Figure 23, that the total asphaltene content, Resin fractions and sulfur contents are the factors controlling the conversion level of the vacuum residues in the commercial ebullated bed vacuum residue hydrocracking operating at the same sediment formation rate.

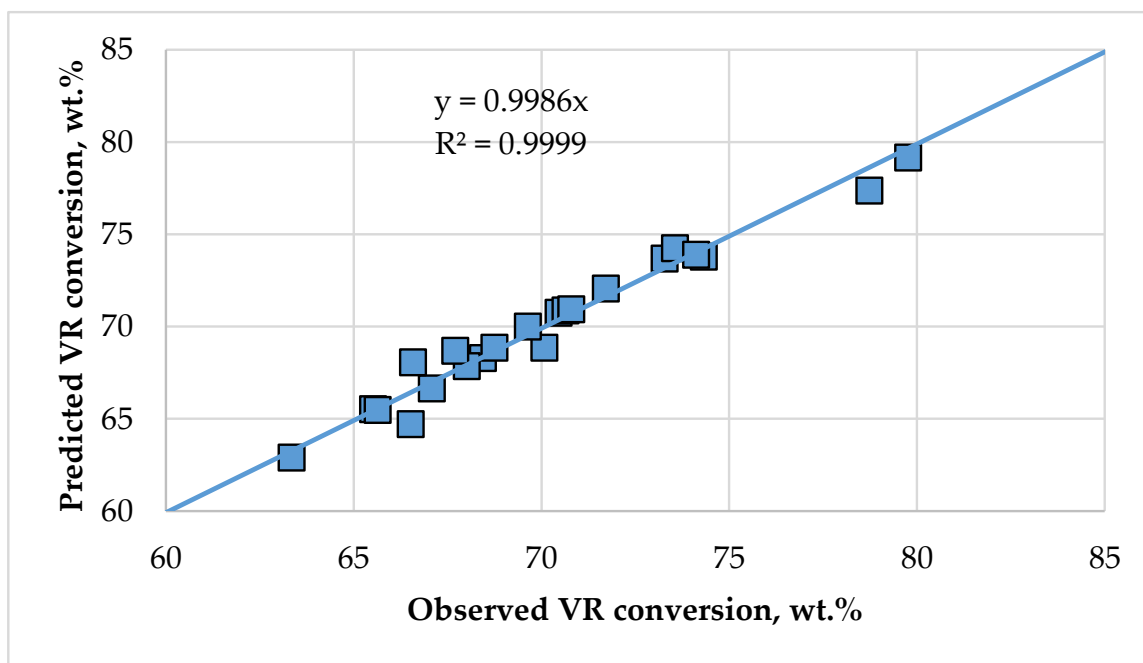


Figure 23. Agreement between observed and predicted by Equation (12) conversion of the straight-run vacuum residues having different SAR-AD fraction compositions.

The effect of sulfur on vacuum residue conversion, as shown in Equation (12), agrees with literature reports. It has been shown that sulfides are some of the most reactive chemical groups and that the rate of cracking is most dependent on their concentration [102], while other studies focus on the total sulfur content of the whole vacuum residue [103,104]. The retardation effect on the conversion of the Resin and total asphaltene content in the vacuum residue during hydrocracking has been previously reported by Guo [9], which showed that the resin and asphaltene fractions are the most refractory components during the thermal cracking of Jinzhou vacuum residue.

Table 8. SAR-AD composition of studied individual straight-run vacuum residues and determined by the use of the approximate linear combination technique conversion levels at the same sediment formation rates observed at the commercial ebullated bed hydrocracker.

Nr	ELSD Data (wt.%)	Sat	Aro-1	Aro-2	Aro-3	Resins	CyC ₆	Toluene	CH ₂ Cl ₂	Total Asph.	VR Sulfur	Conversion, wt.%
1	Arab Medium	9.25	8.04	25.37	37.51	11.01	2.43	6.11	0.28	8.82	5.4	73.3
2	Arab Heavy	6.16	6.84	23.51	36.68	13.59	3.34	9.55	0.33	13.21	5.8	71.7
3	Arab Light	11.32	11.07	28.06	34.76	8.98	1.58	4.01	0.22	5.81	4.9	73.6
4	Basra Light	7.92	6.44	22.66	38.30	14.41	2.81	7.18	0.28	10.27	5.9	74.3
5	Basra Heavy	7.40	6.53	23.90	38.88	13.42	2.98	6.60	0.28	9.86	7.1	78.7
6	Kirkuk	9.52	6.61	23.34	39.16	10.20	2.28	8.39	0.49	11.15	5.9	74.1
7	El-Bouri	14.69	8.32	21.38	33.81	10.15	2.33	8.83	0.49	11.64	3.3	67.1
8	Rhemoura	15.69	7.57	18.52	36.03	11.40	1.90	8.45	0.43	10.78	1.8	63.3
9	CPC	39.63	10.55	18.08	22.38	7.02	0.44	1.64	0.24	2.33	2.1	70.1
10	Azeri Light	34.94	6.90	15.67	30.68	10.67	0.25	0.74	0.13	1.12	0.5	66.5
11	Varandey	31.06	7.14	15.83	27.86	13.08	1.60	3.21	0.20	5.01	1.7	65.5
12	Sib Light	21.15	9.45	19.42	32.17	13.38	1.30	2.94	0.14	4.38	1.6	65.6
13	Urals-2	19.77	7.55	22.73	32.60	11.67	2.04	3.56	0.08	5.68	2.8	68.4
14	Urals-1	18.24	7.04	20.75	33.04	13.98	2.43	4.43	0.09	6.95	3.0	68.0
15	Imported AR	7.96	7.34	26.36	39.33	12.06	2.09	4.71	0.15	6.95	3.3	68.8
16	Prinos	4.61	4.64	17.40	44.84	11.14	1.77	14.94	0.61	17.32	9.1	79.8
17	H-Oil Feed blend 1	14.48	7.55	25.52	36.68	9.75	1.54	4.32	0.16	6.02	2.7	66.6
18	H-Oil Feed blend 2	14.12	6.88	25.80	36.61	9.90	2.03	4.39	0.26	6.68	3.8	70.5
19	H-Oil Feed blend 3	16.13	4.96	24.06	41.60	5.81	0.81	6.27	0.34	7.42	3.0	67.7
20	H-Oil Feed blend 4	17.8	7.4	24.0	33.1	11.0	2.0	4.5	0.1	6.7	3.6	69.6
21	H-Oil Feed blend 5	15.90	7.60	24.58	34.39	10.95	2.14	4.33	0.11	6.58	3.9	70.6
22	H-Oil Feed blend 6	13.95	7.07	25.17	37.60	9.35	2.12	4.63	0.10	6.85	3.9	70.8
23	Boscan	1.55	1.89	12.35	26.60	23.39	8.14	25.57	0.50	34.20	6.0	
24	Albanian	1.20	2.01	17.46	41.53	12.88	5.54	18.65	0.64	24.83	8.7	
25	Tempa Rossa	0.75	2.12	18.35	44.24	10.87	4.48	18.40	0.67	23.55	9.3	

The resin and asphaltene vacuum residue fractions contain the majority of vanadium, nickel, and nitrogen impurities [105–107], which are known to have detrimental effects on catalyst activity [108–115] and consequently on sediment formation rate [108,112]. In our previous studies, the dependence on the Resins fraction was not observed [21,53] when using SARA data obtained according to ASTM D4124. This is because ASTM D4124 produces a very large cut for the polar Aromatics/Resins fractions. This lack of resolution masks differences between feeds with respect to a more defined Resins fraction. For the SAR-AD, the Resins fraction is material from the maltenes, which reversibly adsorbs onto glass beads. When eluted, this fraction is highly brown in color, which can be observed in Figure 1 in the 500 nm data. This is different from the Aro-3 fraction, which has a very low concentration of 500 nm-absorbing molecules. The Resins fraction has a high concentration of compounds that absorb at 500 nm, indicating a significant amount of aromatic conjugation, but also polar heteroatoms that change the electronic pi-electron transition of fused aromatic ring systems to make them more colored. Surface activity (polar heteroatoms) in the Resins fraction is confirmed not only by the fact that this material adsorbs to the glass beads column but also by the model compound study, which showed that polar oxygen and nitrogen functional groups report to this fraction. Furthermore, the model compound study shows that metalated polar vanadium oxide porphyrin compounds preferentially report to the Resins fraction as well as isolated petroleum porphyrins. It should be noted that the high concentration of brown material at 500 nm for the Resins fraction does not carry over to how the asphaltene and maltene separations are performed on the first inert column with heptane. This is inferred from the fact that the amount of heptane asphaltenes produced during the SAR-AD separation is in very good agreement with reported gravimetric heptane asphaltene separations performed on well-characterized Strategic Highway Research Program asphalt binders (vacuum residues) [116]. Figure 24 shows the correlation between the heptane SAR-AD asphaltenes and gravimetric asphaltenes.

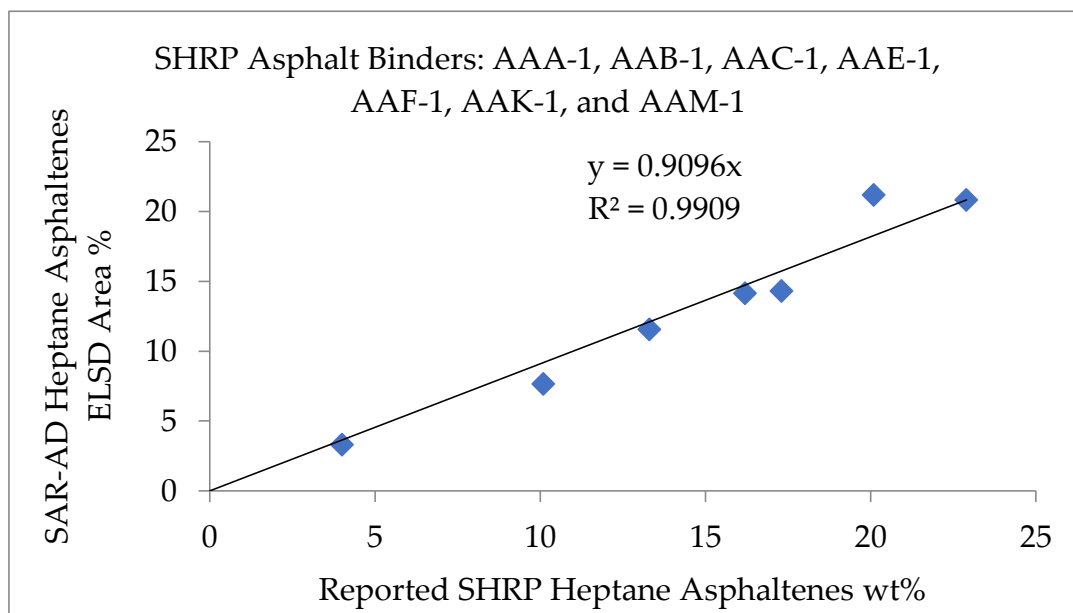


Figure 24. Correlation between SAR-AD heptane asphaltenes and gravimetric heptane asphaltenes for select SHPR core asphalt binders.

Vacuum residues, which are richer in the SAR-AD resins and asphaltene fractions, are expected to exhibit poor performance in the ebullated bed vacuum residue hydrocracking, resulting in a higher sediment formation rate and requiring operation at a lower severity that eventually results in lower conversion.

4. Conclusions

Thirty-four primary and secondary vacuum residual oils were characterized by the Western Research Institute SAR-AD eight-fraction method. On the basis of intercriteria analysis and evaluation, it was shown that the main limitation in the ebullated bed vacuum residue hydrocracking, at a constant sediment formation rate, positively correlates with only two SAR-AD characteristics: toluene asphaltene and total asphaltene content. The content of the Saturates, Aro-1, Aro-2, and Aro-3 fractions in the hydrocracked vacuum residue was found to depend on their contents in the feed and the conversion level. The Resins, CyC₆, and CH₂Cl₂ asphaltene fractions were found to depend only on their content in the ebullated bed vacuum residue feed. The VTB Toluene asphaltene fraction did not show any statistically meaningful relation to its content in the feed or to its conversion level. It seems that the Toluene asphaltene fraction content in the VTB is due to the fraction being an intermediate fraction, produced from the destruction of the Resins fraction and CyC₆ asphaltenes and their subsequent depletion and conversion to CH₂Cl₂ asphaltenes. The Toluene asphaltene content may also depend on the available catalyst active sites, which are governed by the fresh catalyst addition rate. The straight-run vacuum residue conversion at a constant sediment formation rate depends negatively on SAR-AD fractions, resins, and total asphaltenes and positively on the total sulfur content. Non-catalytic coking and mild pyrolysis of Lloydminster asphaltenes and Lloydminster vacuum residue, respectively, show consistency in trends observed with ebullated bed results.

SAR-AD model compound and thermal cracking results helped to explain why the Aro-3 fraction increases with conversion, relative to the other maltene fractions. This is mostly due to the large size and refractory nature of the 4+ fused aromatic ring structures in this fraction. Model compounds also show that polar functional groups and metallated porphyrins are present in the SAR-AD Resins fraction. This explains why the Resins fraction also contributed to lowering conversion levels during hydrocracking despite being good at stabilizing asphaltenes.

The correlations developed in this study can be used to evaluate the effect of the vacuum residues derived from different crude oils on the performance of the ebullated bed hydrocracking in the process of crude oil selection.

Author Contributions: Conceptualization, J.J.A.; methodology, J.F.R. and J.J.A.; software, S.N., S.R. and D.S.; formal analysis, I.S., J.L., A.L. and J.H.; investigation, I.K., D.S., J.J.A., G.P. and J.-P.P.; resources, K.A. and J.J.A.; data curation, D.Y.; writing—original draft preparation, J.J.A.; writing—review and editing, J.J.A.; supervision, K.A.; project administration, J.J.A.; funding acquisition, J.F.R. and J.J.A. All authors have read and agreed to the published version of the manuscript.

Funding: Funding for the SAR-AD model compound study was provided by the University of Wyoming School of Energy Resources through the Carbon Initiative and Carbon Engineering program.

Data Availability Statement: Not applicable.

Acknowledgments: The authors, Krassimir Atanassov and Simeon Ribagin, acknowledge the support from the Bulgarian National Science Fund under Grant Ref. No. KP-06-N22-1/2018 “Theoretical research and applications of InterCriteria Analysis”.

Conflicts of Interest: The authors declare no conflict of interest.

Nomenclature

SAR-AD TM	Saturates, aromatics, and resins—Asphaltene Determinator;
SARA	Saturates, aromatics, resins, and asphaltenes;
TLC/FID	Thin layer chromatography/flame ionization detection;
HPLC	High performance liquid chromatography;
ARO	Aromatics;
ELSD	Evaporative light scattering detector;
AD	Asphaltene Determinator;
CH ₂ Cl ₂	Dichloromethane;

CyC6	Cyclohexane;
ASTM	American Society for Testing and Materials;
LNB	Lukoil Neftochim Bourgas;
TBP	True boiling point;
HTSD	High temperature simulated distillation;
VR	Vacuum residue;
FCC HCO	Fluid Catalytic Cracking Heavy Cycle Oil;
H-Oil	Ebullated bed hydrocracking;
CII	Colloidal instability index;
MCII	Modified colloidal instability index;
MI	Maltenes Index;
SAT	Saturated;
PAH	Polycyclic aromatic hydrocarbons;
STM-AFM	Scanning tunneling microscopy coupled with atomic force microscopy;
FCC	Fluid Catalytic Cracking;
TSE	Total sediment existent
ATB	Atmospheric tower bottom;
LHSV	Liquid hourly space velocity, h ⁻¹ ;
VTB	Vacuum tower bottom;
IcrA	Intercriteria analysis;
D15	Density at 15 °C, g/m ³ ;
CCR	Conradson carbon content, wt.%;
C7 asp.	n-heptane asphaltenes, wt.%;
C5 asp.	n-pentane asphaltenes, wt.%;
VIS	kin. viscosity at 80 °C of the blend: 70% VR/30% fluid catalytic cracking heavy cycle oil;
Crude T50%	Boiling point of 50% of the evaporate from the crude oil, °C;
VR T50%	Boiling point of 50% of the evaporate from the vacuum residue fraction, °C;
TRX	Weight average bed temperature, °C.

References

- Stratiev, D.; Shishkova, I.; Marinov, I.; Nikolaychuk, E.; Nedelchev, A.; Ivanova, N.; Yordanov, D.; Tankov, I.; Mitkova, M.; Stanulov, K.; et al. Effect of feedstock origin on conversion and yields of products from the ebullated bed vacuum residue hydrocracker. *Neftopererab. I Neft*. **2017**, *10*, 3–13.
- Prajapati, R.; Kohli, K.; Maity, S.K. Residue upgradation with slurry phase catalyst: Effect of feedstock properties. *Fuel* **2019**, *239*, 452–460. [\[CrossRef\]](#)
- Zhou, X.-L.; Chen, S.-Z.; Li, C.A. A predictive kinetic model for delayed coking. *Pet. Sci. Technol.* **2007**, *25*, 1539–1548. [\[CrossRef\]](#)
- Ghashghaee, M. Thorough assessment of delayed coking correlations against literature data: Development of improved alternative models. *React. Kinet. Mech. Catal.* **2019**, *126*, 83–102. [\[CrossRef\]](#)
- Muñoz, J.A.D.; Aguilar, R.; Castañeda, L.C.; Ancheyta, J. Comparison of correlations for estimating product yields from delayed coking. *Energy Fuels* **2013**, *27*, 7179–7190. [\[CrossRef\]](#)
- Redelius, P.; Soenen, H. Relation between bitumen chemistry and performance. *Fuel* **2015**, *27*, 7179–7190. [\[CrossRef\]](#)
- Stratiev, D.S.; Shishkova, I.K.; Dinkov, R.K.; Petrov, I.P.; Kolev, I.V.; Yordanov, D.; Sotirov, S.; Sotirova, E.; Atanassova, V.; Ribagin, S.; et al. Empirical Models to Characterize the Structural and Physiochemical Properties of Vacuum Gas Oils with Different Saturate Contents. *Resources* **2021**, *10*, 71. [\[CrossRef\]](#)
- Corbett, L.W. Composition of asphalt based on generic fractionation, using solvent deasphalting, elution-adsorption chromatography, and densimetric characterization. *Anal. Chem.* **1969**, *41*, 576–579. [\[CrossRef\]](#)
- Guo, A.; Zhang, X.; Wang, Z. Simulated delayed coking characteristics of petroleum residues and fractions by thermogravimetry. *Fuel Process. Technol.* **2008**, *89*, 643–650. [\[CrossRef\]](#)
- Liu, C.; Zhu, C.; Jin, L.; Shen, R.; Liang, W. Step by step modeling for thermal reactivities and chemical compositions of vacuum residues and their SFEF asphalts. *Fuel Process. Technol.* **1999**, *59*, 51–67. [\[CrossRef\]](#)
- Schucker, R.C. Thermogravimetric determination of the coking kinetics of Arab Heavy vacuum residuum. *Ind. Eng. Chem. Process Des. Dev.* **1983**, *22*, 615–619. [\[CrossRef\]](#)
- Russell, C.A.; Crozier, S.; Sharpe, R. Observations from heavy residue pyrolysis: A novel method to characterize fouling potential and assess antifoulant additive performance. *Energy Fuels* **2010**, *24*, 5483–5492. [\[CrossRef\]](#)
- Yang, C.; Du, F.; Zheng, H.; Keng, H.C. Hydroconversion characteristics and kinetics of residue narrow fractions. *Fuel* **2005**, *84*, 675–684. [\[CrossRef\]](#)

14. Stratiev, D.; Shishkova, I.; Dinkov, R.; Nikolova, R.; Mitkova, M.; Stanulov, K.; Sharpe, R.; Russell, C.A.; Obryvalina, A.; Telyashev, R. Reactivity and stability of vacuum residual oils in their thermal conversion. *Fuel* **2014**, *123*, 133–142. [\[CrossRef\]](#)
15. Félix, G.; Ancheyta, J. Comparison of hydrocracking kinetic models based on SARA fractions obtained in slurry-phase reactor. *Fuel* **2019**, *241*, 495–505. [\[CrossRef\]](#)
16. Xu, C.; Gao, J.; Zhao, S.; Lin, S. Correlation between feedstock SARA components and FCC product yields. *Fuel* **2005**, *84*, 669–674. [\[CrossRef\]](#)
17. Alvarez, E.; Marroquin, G.; Trejo, F.; Centeno, G.; Ancheyta, J.; Diaz, J. Pyrolysis kinetics of atmospheric residue and its SARA fractions. *Fuel* **2011**, *90*, 3602–3607. [\[CrossRef\]](#)
18. Hauser, A.; Alhumaidan, F.; Al-Rabiah, H.; Halabi, M.A. Study on thermal cracking of Kuwaiti heavy oil (vacuum residue) and its SARA fractions by NMR spectroscopy. *Energy Fuels* **2014**, *28*, 4321–4332. [\[CrossRef\]](#)
19. Xia, W.; Xu, T. Thermal characteristics, kinetic models, and volatile constituents during the energy conversion of bituminous SARA Fractions in air. *ACS Omega* **2020**, *5*, 20831–20841. [\[CrossRef\]](#)
20. Alonso-Ramirez, G.; Cuevas-Garcia, R.; Sanchez-Minero, F.; Ramirez, J.; Moreno-Montiel, M.; Ancheyta, J.; Carbajal-Vielman, R. Catalytic hydrocracking of a Mexican heavy oil on a MoS₂/Al₂O₃ catalyst: I. Study of the transformation of isolated saturates fraction obtained from SARA analysis. *Catal. Tod.* **2020**, *353*, 153–162. [\[CrossRef\]](#)
21. Stratiev, D.; Shishkova, I.; Kolev, I.; Yordanov, D.; Toteva, V. Petroleum crude slate effect on H-Oil performance. *Int. J. Oil Gas Coal Technol.* **2021**, *28*, 259–286. [\[CrossRef\]](#)
22. Santos, J.M.; Vetere, A.; Wisniewski, A.; Eberlin, M.N.; Schrader, W. Modified SARA method to unravel the complexity of resin fraction(s) in crude oil. *Energy Fuels* **2020**, *34*, 16006–16013. [\[CrossRef\]](#)
23. Zhang, J.; Tian, Y.; Qiao, Y.; Yang, C.S.H. Structure and reactivity of Iranian vacuum residue and its eight group-fractions. *Energy Fuels* **2017**, *31*, 8072–8086. [\[CrossRef\]](#)
24. Che, Y.; Yang, Z.; Qiao, Y.; Zhang, J.; Tian, Y. Study on pyrolysis characteristics and kinetics of vacuum residue and its eight group-fractions by TG-FTIR. *Thermochim. Acta* **2018**, *669*, 149–155. [\[CrossRef\]](#)
25. Zhang, J.; Niwamanya, N.; Gao, C.; Sekyere, D.T.; Barigye, A.; Tian, Y. Structure and millisecond pyrolysis behavior of heavy oil and its eight group-fractions on solid base catalyst. *Fuel* **2022**, *318*, 123483. [\[CrossRef\]](#)
26. Jiang, C.; Larter, S.R.; Noke, K.J.; Snowden, L.R. TLC–FID (Iatroscan) analysis of heavy oil and tar sand samples. *Org. Geochem.* **2008**, *39*, 1210–1214. [\[CrossRef\]](#)
27. Liang, W.; Que, G.H.; Chen, Y. Chemical composition and structure of vacuum residues of Chinese crudes I. Chemical composition of vacuum residues. *Acta Pet. Sin. (Pet. Process. Sect.)* **1991**, *7*, 1–7.
28. Masson, J.-F.; Price, T.; Collins, P. Dynamics of bitumen fractions by thin-layer chromatography/flame ionization detection. *Energy Fuels* **2001**, *15*, 955–960. [\[CrossRef\]](#)
29. Schabron, J.F.; Gardner, G.W.; Hart, J.K.; Niss, N.D. The Characterization of Petroleum Residua. *West. Res. Inst. Rep.* **1993**. Report to Mobil Research and Development Corp. and DOE. DOE Report DOE/MC/11076-3539.
30. Woods, J.; Kung, J.; Kingston, D.; Kotlyar, L.; Sparks, B.; McCracken, T. Canadian crudes: A comparative study of SARA fractions from a modified HPLC separation technique. *Oil Gas Sci. Technol.* **2008**, *63*, 151–163. [\[CrossRef\]](#)
31. ASTM D2007; Standard Test Method for Characteristic Groups in Rubber Extender and Processing Oils and Other Petroleum-Derived Oils by the Clay-Gel Absorption Chromatographic Method. ASTM: West Conshohocken, PA, USA, 2016.
32. ASTM D4124-09; Standard Test Method for Separation of Asphalt into Four Fractions. ASTM: West Conshohocken, PA, USA, 2009.
33. Thenoux, G.; Bell, C.A.; Wilson, J.E.; Eakin, D.; Schroeder, M. Experiences with the Corbett-Swarbrick procedure for separation of asphalt into four generic fractions. *Transp. Res. Rec.* **1988**, *1171*, 66–70.
34. Bissada, K.K.; Tan, J.; Szymczyk, E.; Darnell, M.; Mei, M.; Zhou, J. Group-type characterization of crude oil and bitumen. Part I: Enhanced separation and quantification of saturates, aromatics, resins and asphaltenes (SARA). *Org. Geochem.* **2016**, *95*, 21–28. [\[CrossRef\]](#)
35. Huang, Y.S.; You, H.Q.; Zhou, X.P.; Guitarte, J.; Xian, C.; Liu, W.; Chen, X.; Guo, H. Cased hole formation testing in very challenging operational conditions reveals mystery of reservoir—A case study in South China Sea. In Proceedings of the International Petroleum Technology Conference, Bangkok, Thailand, 7–9 February 2011.
36. Stratiev, D.; Shishkova, I.; Nikolova, R.; Tsaneva, T.; Mitkova, M.; Yordanov, D. Investigation on precision of determination of SARA analysis of vacuum residual oils from different origin. *Pet. Coal.* **2016**, *58*, 109–119.
37. Fuhr, B.J.; Hawrelechko, C.; Holloway, L.R.; Huang, H. Comparison of bitumen fractionation methods. *Energy Fuels* **2005**, *19*, 1327–1329. [\[CrossRef\]](#)
38. Adams, J.; Elwardany, M.; Planche, J.-P.; Boysen, R.; Rovani, J. Diagnostic techniques for various asphalt refining and modification methods. *Energy Fuels* **2019**, *33*, 2680–2698. [\[CrossRef\]](#)
39. Adams, J.J.; Schabron, J.F.; Boysen, R. Quantitative vacuum distillation of crude oils to give residues amenable to the asphaltene determinator coupled with saturates, aromatics, and resins separation characterization. *Energy Fuels* **2015**, *29*, 2774–2784. [\[CrossRef\]](#)
40. Boysen, R.; Schabron, J.F. The automated asphaltene determinator coupled with saturates, aromatics, and resins separation for petroleum residua characterization. *Energy Fuels* **2013**, *27*, 4654–4661. [\[CrossRef\]](#)

41. Kharrat, A.M.; Zacharia, J.; Cherian, V.J.; Anyatonwu, A. Issues with comparing SARA methodologies. *Energy Fuels* **2007**, *21*, 3618–3621. [\[CrossRef\]](#)
42. Todorova-Yankova, L.; Yordanov, D.; Stratiev, D.; Shishkova, I. Investigation of the group hydrocarbon composition of vacuum residues from different types of crude oil, crude oil sands and bitumens. *Ind. Technol.* **2021**, *8*, 51–64.
43. Efimov, I.; Povarov, V.G.; Rudko, V.A. Comparison of UNIFAC and LSER models for calculating partition coefficients in the hexane–acetonitrile system using middle distillate petroleum products as an example. *Ind. Eng. Chem. Res.* **2022**, *61*, 9575–9585. [\[CrossRef\]](#)
44. Efimov, I.; Povarov, V.G.; Rudko, V.A. Use of partition coefficients in a hexane–Acetonitrile system in the GC–MS analysis of polyaromatic hydrocarbons in the example of delayed coking gas oils. *ACS Omega* **2021**, *6*, 9910–9919. [\[CrossRef\]](#) [\[PubMed\]](#)
45. Smyshlyaeva, K.I.; Rudko, V.A.; Kuzmin, K.A.; Vladimir, G.; Povarov, V.G. Asphaltene genesis influence on the low-sulfur residual marine fuel sedimentation stability. *Fuel* **2022**, *328*, 125291. [\[CrossRef\]](#)
46. Ershov, M.A.; Savelenko, V.D.; Makhmudova, A.E.; Rekhletskaia, E.S.; Makhova, U.A.; Kapustin, V.M.; Mukhina, D.Y.; Abdellatief, T.M.M. Technological Potential Analysis and Vacant Technology Forecasting in Properties and Composition of Low-Sulfur Marine Fuel Oil (VLSFO and ULSFO) Bunkered in Key World Ports. *J. Mar. Sci. Eng.* **2022**, *10*, 1828. [\[CrossRef\]](#)
47. Félix, G.; Tirado, A.; Al-Muntaser, A.; Kwofie, M.; Varfolomeev, M.A.; Yuan, C.; Ancheyta, J. SARA-based kinetic model for non-catalytic aquathermolysis of heavy crude oil. *J. Pet. Sci. Eng.* **2022**, *216*, 110845. [\[CrossRef\]](#)
48. Rakhmatullin, I.; Efimov, S.; Tyurin, V.; Gafurov, M.; Al-Muntaser, A.; Varfolomeev, M.; Klochov, V. Qualitative and quantitative analysis of heavy crude oil samples and their SARA fractions with ¹³C nuclear magnetic resonance. *Processes* **2020**, *8*, 995. [\[CrossRef\]](#)
49. Stratiev, D.; Shishkova, I.; Tankov, I.; Pavlova, A. Challenges in characterization of residual oils. A review. *J. Petrol. Sci. Eng.* **2019**, *178*, 227–250. [\[CrossRef\]](#)
50. Schabron, J.F.; Rovani, J.F. On-column precipitation and re-dissolution of asphaltenes in petroleum residua. *Fuel* **2008**, *87*, 165–176. [\[CrossRef\]](#)
51. Schabron, J.F.; Rovani, J.F.; Sanderson, M. Asphaltene determinator method for automated on-column precipitation and redissolution of pericondensed aromatic asphaltene components. *Energy Fuels* **2010**, *24*, 5984–5996. [\[CrossRef\]](#)
52. Schabron, J.F.; Pauli, A.T.; Rovani, J.F.; Miknis, F.P. Predicting Coke Formation Tendencies. *Fuel* **2001**, *80*, 1435–1446. [\[CrossRef\]](#)
53. Stratiev, D.; Nenov, S.; Shishkova, I.; Georgiev, B.; Argirov, G.; Dinkov, R.; Yordanov, D.; Atanassova, V.; Vassilev, P.; Atanassov, K. Commercial investigation of the ebullated-bed vacuum residue hydrocracking in the conversion range of 55–93%. *ACS Omega* **2020**, *51*, 33290–33304. [\[CrossRef\]](#)
54. Stratiev, D.; Nenov, S.; Nedanovski, D.; Shishkova, I.; Dinkov, R.; Stratiev, D.D.; Sotirov, S.; Sotirova, E.; Atanassova, V.; Ribagin, S.; et al. Empirical modeling of viscosities and softening points of straight-run vacuum residues from different origins and of hydrocracked unconverted vacuum residues obtained in different conversions. *Energies* **2022**, *15*, 1755. [\[CrossRef\]](#)
55. Stratiev, D.; Dinkov, R.; Shishkova, I.; Sharafutdinov, I.; Ivanova, N.; Mitkov, M.; Yordanov, D.; Rudnev, N.; Stanulov, K.; Artemiev, A.; et al. What is behind the high values of hot filtration test of the ebullated bed residue H-Oil hydrocracker residual oils. *Energy Fuels* **2016**, *30*, 7037–7054. [\[CrossRef\]](#)
56. Stratiev, D.S.; Shishkova, I.K.; Dinkov, R.K.; Petrov, I.P.; Kolev, I.V.; Yordanov, D.; Sotirov, S.; Sotirova, E.N.; Atanassova, V.K.; Ribagin, S.; et al. Crude slate, FCC slurry oil, recycle, and operating conditions effects on H-Oil product quality. *Processes* **2021**, *9*, 952. [\[CrossRef\]](#)
57. Zhang, Y.; Schulz, F.B.; Rytting, F.M.; Walters, C.C.; Kaiser, K.; Metz, J.N.; Harper, M.R.; Merchant, S.S.; Mennito, A.S.; Qian, K.J.; et al. Elucidating the geometric substitution of petroporphyrins by spectroscopic analysis and atomic force microscopy molecular imaging. *Energy Fuels* **2019**, *33*, 6088–6097. [\[CrossRef\]](#) [\[PubMed\]](#)
58. Schabron, J.F.; Pauli, A.T., Jr.; Rovani, J.F. Residua Coke Formation Predictability Maps. *Fuel* **2002**, *81*, 2227–2240. [\[CrossRef\]](#)
59. Jover, J.; Cirera, J. Computational assessment on the Tolman cone angles for P-ligands. *Dalton Trans.* **2019**, *48*, 15036. [\[CrossRef\]](#)
60. Schuler, B.; Meyer, G.; Peña, D.; Mullins, O.C.; Gross, L. Unraveling the molecular structures of asphaltenes by atomic force microscopy. *J. Am. Chem. Soc.* **2015**, *137*, 9870–9876. [\[CrossRef\]](#)
61. Zhang, Y.; Schuler, B.; Fatayer, S.; Gross, L.; Harper, M.R.; Kushnerick, J.D. Understanding the effects of sample preparation on the chemical structures of petroleum imaged with non-contact atomic force microscopy. *Ind. Eng. Chem. Res.* **2018**, *57*, 15935–15941. [\[CrossRef\]](#)
62. Chen, P.; Metz, J.N.; Mennito, A.S.; Merchant, S.; Smith, S.E.; Siskin, M.; Ricker, S.P.; Dankworth, D.C.; Kushnerick, J.D.; Yao, N.; et al. Petroleum Pitch: Exploring a 50-year structure puzzle with real-space molecular imaging. *Carbon* **2020**, *161*, 456–465. [\[CrossRef\]](#)
63. Zhang, Y. Applications of Noncontact Atomic Force Microscopy in Petroleum Characterization: Opportunities and Challenges. *Energy Fuels* **2021**, *35*, 14422–14444. [\[CrossRef\]](#)
64. Stanislaus, A.; Hauser, A.; Marafi, M. Investigation of the mechanism of sediment formation in residual oil hydrocracking process through characterization of sediment deposits. *Catal. Today* **2005**, *109*, 167–177. [\[CrossRef\]](#)
65. Pang, W.W.; Kuramae, M.; Kinoshita, Y.; Lee, J.K.; Zhang, Y.Z.; Yoon, S.H.; Mochida, I. Plugging problems observed in severe hydrocracking of vacuum residue. *Fuel* **2009**, *88*, 663–669. [\[CrossRef\]](#)
66. Stratiev, D.; Shishkova, I.; Nikolaychuk, E.; Ilchev, I.; Yordanov, D. Investigation of the effect of severity mode of operation in the H-Oil vacuum residue hydrocracking on sediment formation during processing different feeds. *Pet. Coal* **2020**, *62*, 50–62.

67. Stratiev, D.; Shishkova, I.; Dinkov, R.; Kolev, I.; Argirov, G.; Ivanov, V.; Ribagin, S.; Atanassova, V.; Atanassov, K.; Stratiev, D.D.; et al. InterCriteria analysis to diagnose the reasons for increased fouling in a commercial ebullated bed vacuum residue hydrocracker. *ACS Omega* **2022**, *7*, 30462–30476. [\[CrossRef\]](#)
68. Stratiev, D.; Shishkova, I.; Nedelchev, A.; Kirilov, K.; Nikolaychuk, E.; Ivanov, A.; Sharafutdinov, I.; Veli, A.; Mitkova, M.; Tsaneva, T.; et al. Investigation of relationships between petroleum properties and their impact on crude oil compatibility. *Energy Fuels* **2015**, *29*, 7836–7854. [\[CrossRef\]](#)
69. Mavrov, D. Software for interCriteria analysis: Implementation of the main algorithm. *Notes Intuit. Fuzzy Sets* **2015**, *21*, 77–86.
70. Mavrov, D. Software for interCriteria analysis: Working with the results. *Annu. Inform. Sect. Union Sci. Bulg.* **2015**, *8*, 37–44.
71. Mavrov, D.; Radeva, I.; Atanassov, K.; Doukovska, L.; Kalaykov, I. InterCriteria software design: Graphic interpretation within the intuitionistic fuzzy triangle. In Proceedings of the Fifth International Symposium on Business Modeling and Software Design, Fribourg, Switzerland, 5–7 July 2015; pp. 279–283.
72. Ikonov, N.; Vassilev, P.; Roeva, O. Software for interCriteria analysis. *Int. J. Bioautomation* **2018**, *22*, 1–10. [\[CrossRef\]](#)
73. Bannayan, M.A.; Lemke, H.K.; Stephenson, W.K. Fouling mechanisms and effect of process conditions on deposit formation in H-Oil. *Stud. Surf. Sci. Catal.* **1996**, *100*, 273–281.
74. Rogel, E.; Ovalles, C.; Moir, M. Asphaltene chemical characterization as a function of solubility: Effects on stability and aggregation. *Energy Fuels* **2012**, *26*, 2655–2662. [\[CrossRef\]](#)
75. Mochida, I.; Zhao, Z.; Sakanishi, K.; Yamamoto, S.; Takashima, H.; Uemura, S.V. Structure and properties of sludges produced in the catalytic hydrocracking of vacuum residue. *Ind. Eng. Chem. Res.* **1989**, *28*, 418–421.
76. Ovalles, C.; Rogel, E.; Moir, M.E.; Brait, A. Hydroprocessing of vacuum residues: Asphaltene characterization and solvent extraction of spent slurry catalysts and the relationships with catalyst deactivation. *Appl. Catal. A Gen.* **2016**, *532*, 57–64. [\[CrossRef\]](#)
77. Manek, E.; Haydary, J. Hydrocracking of vacuum residue with solid and dispersed phase catalyst: Modeling of sediment formation and hydrodesulfurization. *Fuel Process. Technol.* **2017**, *159*, 320–327.
78. Rogel, E.; Ovalles, C.; Pradhan, A.; Leung, P.; Chen, N. Sediment formation in residue hydroconversion processes and its correlation to asphaltene behavior. *Energy Fuels* **2013**, *27*, 6587–6593. [\[CrossRef\]](#)
79. Felix, G.; Ancheyta, J. Using separate kinetic models to predict liquid, gas, and coke yields in heavy oil hydrocracking. *Ind. Eng. Chem. Res.* **2019**, *58*, 7973–7979. [\[CrossRef\]](#)
80. Gaulier, F.; Barbier, J.; Guichard, B.; Levitz, P.; Espinat, D. Asphaltenes transport into catalysts under hydroprocessing conditions. *Energy Fuels* **2015**, *29*, 6250–6258. [\[CrossRef\]](#)
81. Kim, C.H.; Hur, Y.G.; Lee, K.Y. Relationship between surface characteristics and catalytic properties of unsupported nickel-tungsten carbide catalysts for the hydrocracking of vacuum residue. *Fuel* **2022**, *309*, 122103. [\[CrossRef\]](#)
82. Nguyen, N.T.; Kang, K.H.; Pham, H.H.; Go, K.S.; Pham, D.V.; Seo, P.W.; Nho, N.S.; Chul, W.; Sunyoung, P. Catalytic hydrocracking of vacuum residue in a semi-batch reactor: Effect of catalyst concentration on asphaltene conversion and product distribution. *J. Ind. Eng. Chem.* **2021**, *102*, 112–121. [\[CrossRef\]](#)
83. Lim, S.H.; Go, K.S.; Nho, N.S.; Kim, Y.K.; Kwon, E.H.; Kwang, K.; Lee, J. Reaction characteristics and sediment formation of slurry phase hydrocracking with vacuum residue in a bench-scale bubble column reactor. *J. Petrol. Sci. Eng.* **2021**, *196*, 107713. [\[CrossRef\]](#)
84. Lim, S.H.; Go, K.S.; Kwon, E.H.; Nho, N.S.; Lee, J.G. Investigation of asphaltene dispersion stability in slurry-phase hydrocracking reaction. *Fuel* **2020**, *271*, 117509. [\[CrossRef\]](#)
85. Lim, S.H.; Go, K.S.; Nho, N.S.; Lee, J.G. Effect of reaction temperature and time on the products and asphaltene dispersion stability in slurry-phase hydrocracking of vacuum residue. *Fuel* **2018**, *234*, 305–311. [\[CrossRef\]](#)
86. Lim, S.H.; Go, K.S.; Nho, N.S.; Lee, J.G. Effect of aromatic additives on the coke reduction and the asphaltene conversion in a slurry-phase hydrocracking. *Korean Chem. Eng. Res.* **2019**, *57*, 244–252.
87. Du, H.; Liu, D.; Liu, H.; Gao, P.; Lv, R.; Li, M.; Lou, B.; Yang, Y. Role of hydrogen pressure in slurry-phase hydrocracking of Venezuela heavy oil. *Energy Fuels* **2015**, *29*, 2104–2110. [\[CrossRef\]](#)
88. Chabot, J.; Shiflett, W. Residuum hydrocracking: Chemistry and catalysis. *PTQ* **2019**, *Q3*, 1–9.
89. Mochida, I.; Korai, Y.; Hieida, T.; Azuma, A.; Kitajima, E. Detailed analyses of FCC decant oil as a starting feedstock for mesophase pitch. *Fuel Sci. Technol. Int.* **1991**, *9*, 485–504. [\[CrossRef\]](#)
90. Chacón-Patiño, M.L.; Gray, M.R.; Rüger, C.; Smith, D.F.; Glatke, T.J.; Niles, S.F.; Neumann, A.; Weisbrod, C.R.; Yen, A.; McKenna, A.M.; et al. Lessons learned from a decade-long assessment of asphaltenes by ultrahigh-resolution mass spectrometry and implications for complex mixture analysis. *Energy Fuels* **2021**, *35*, 16335–16376. [\[CrossRef\]](#)
91. Chacón-Patiño, M.L.; Rowland, S.M.; Rodgers, R.P. Advances in asphaltene petroleomics. Part 1: Asphaltenes are composed of abundant island and archipelago structural motifs. *Energy Fuels* **2017**, *31*, 13509–13518. [\[CrossRef\]](#)
92. Chacón-Patiño, M.L.; Rowland, S.M.; Rodgers, R.P. Advances in asphaltene petroleomics. Part 2: Selective separation method that reveals fractions enriched in island and archipelago structural motifs by mass spectrometry. *Energy Fuels* **2018**, *32*, 314–328. [\[CrossRef\]](#)
93. Chacón-Patiño, M.L.; Rowland, S.M.; Rodgers, R.P. Advances in asphaltene petroleomics. Part 3. Dominance of island or archipelago structural motif is sample dependent. *Energy Fuels* **2018**, *32*, 9106–9120. [\[CrossRef\]](#)

94. Chacón-Patiño, M.L.; Smith, D.F.; Hendrickson, C.L.; Marshall, A.G.; Rodgers, R.P. Advances in asphaltene petroleomics. Part 4. Compositional trends of solubility subfractions reveal that polyfunctional oxygen-containing compounds drive asphaltene chemistry. *Energy Fuels* **2020**, *34*, 3013–3030. [\[CrossRef\]](#)
95. Adams, J.; Rovani, J.; Boysen, R.; Elwardany, M.; Planche, J.-P. Innovations and developments in bitumen composition analysis. In Proceedings of the 7th Eurasphalt and Eurobitumen Congress, Virtual, Madrid, Spain, 15–17 June 2021.
96. Petersen, J.C. *A Review of the Fundamentals of Asphalt Oxidation: Chemical, Physicochemical, Physical Property and Durability Relationships*; Transportation Research Board: Washington, DC, USA, 2009.
97. Petersen, J.C.; Glaser, R. Asphalt oxidation mechanisms and the role of oxidation products on age hardening revisited. *Road Mater. Pavement Des.* **2011**, *12*, 795–819. [\[CrossRef\]](#)
98. Mitkova, M.; Stratiev, D.; Shishkova, I.; Dobrev, D. *Thermal and Thermo Catalytic Processes for Heavy Oil Conversion*; Professor Marin Drinov Publishing House of Bulgarian Academy of Sciences: Sofia, Bulgaria, 2017.
99. Stratiev, D.; Shishkova, I.; Dinkov, R.; Dobrev, D.; Argirov, G.; Yordanov, D. The Synergy between ebullated bed vacuum residue hydrocracking and fluid catalytic cracking processes in modern refining—Commercial experience. *Profr. Mar. Drinov Publ. House Bulg. Acad. Sci.* **2022**, 1–750.
100. Harding, R.H.; Zhao, X.; Qian, K.; Rajagopalan, K.; Cheng, W.C. The fluid catalytic cracking selectivities of gas oil boiling point and hydrocarbon fractions. *Prep. Am. Chem. Soc. Div. Pet. Chem.* **1995**, *40*, 762–767. [\[CrossRef\]](#)
101. Harding, R.H.; Zhao, X.; Qian, K.; Rajagopalan, K.; Cheng, W.C. The fluid catalytic cracking selectivities of gas oil boiling point and hydrocarbon fractions. *Ind Eng Chem Res.* **1996**, *35*, 2561–2569. [\[CrossRef\]](#)
102. Saxena, A.; Diaz-Goano, C.; Dettman, H. Coking behavior during visbreaking. *J. Can. Petrol. Technol.* **2012**, *51*, 457–463. [\[CrossRef\]](#)
103. Gray, M.; Chacón-Patiño, M.; Rodgers, R. Structure–Reactivity Relationships for petroleum asphaltenes. *Energy Fuels* **2022**, *36*, 4370–4380. [\[CrossRef\]](#)
104. Guitian, J.; Souto, A.; Ramirez, R.; Marzin, R.; Solari, B. Commercial design of a new upgrading process, HDH. In *proceedings international symposium on Heavy Oil and Residue Upgrading and Utilization*; Han, C., Hsi, C., Eds.; International Academic: Beijing, China, 1992; pp. 237–247.
105. Reynolds, J.G. Characterization of heavy residua by application of a modified D 2007 separation and electron paramagnetic resonance. *Liq. Fuels Technol.* **1985**, *3*, 73–105. [\[CrossRef\]](#)
106. Speight, J.G. Petroleum asphaltenes Part 2 The effect of asphaltenes and resin constituents on recovery and refining processes. *Oil Gas Sci. Technol.* **2004**, *59*, 479–488. [\[CrossRef\]](#)
107. Speight, J.G. Petroleum asphaltenes Part 1. Asphaltenes, resins and the structure of petroleum. *Oil Gas Sci. Technol.* **2004**, *59*, 467–477. [\[CrossRef\]](#)
108. Kohli, K.; Prajapati, R.; Maity, S.K.; Sau, M.; Sharma, B.K. Deactivation of a hydrotreating catalyst during hydroprocessing of synthetic crude by metal bearing compounds. *Fuel* **2019**, *243*, 579–589. [\[CrossRef\]](#)
109. Zhou, J.; Zhao, J.; Zhang, J.; Zhang, T.; Ye, M.; Liu, Z. Regeneration of catalysts deactivated by coke deposition: A review. *Chin. J. Catal.* **2020**, *41*, 1048–1061. [\[CrossRef\]](#)
110. Furimsky, E.; Massoth, F.E. Deactivation of hydroprocessing catalysts. *Catal. Today* **1999**, *52*, 381–495. [\[CrossRef\]](#)
111. Gualda, G.; Kasztelan, S. Coke versus metal deactivation of residue hydrodemetallization catalysts. *Stud. Surf. Sci. Catal.* **1994**, *88*, 145–154.
112. Vogelaar, B.M.; Eijsbouts, S.; Bergwerff, J.A.; Heiszwolf, J. Hydroprocessing catalyst deactivation in commercial practice. *Catal. Today* **2010**, *154*, 256–263. [\[CrossRef\]](#)
113. Nguyen, M.T.; Nguyen, D.L.T.; Changlei, X.; Nguyen, T.B.; Shokouhimehr, M.; Sana, S.S.; NirmalaGrace, A.; Aghbashlo, M.; Tabatabaei, M.; Sonne, C.; et al. Recent advances in asphaltene transformation in heavy oil hydroprocessing: Progress, challenges, and future perspectives. *Fuel Proc. Technol.* **2021**, *213*, 106681. [\[CrossRef\]](#)
114. Gawel, I.; Bociarska, D.; Biskupski, P. Effect of asphaltenes on hydroprocessing of heavy oils and residua. *Appl. Catal. A Gen.* **2005**, *295*, 89–94. [\[CrossRef\]](#)
115. Rana, M.S.; Ancheyta, J.; Sahoo, S.K.; Rayo, P. Carbon and metal deposition during the hydroprocessing of Maya crude oil. *Catal. Today* **2014**, *220*, 97–105. [\[CrossRef\]](#)
116. Jones, D.R. *SHRP Materials Reference Library: Asphalt Cements: A Concise Data Compilation*; Report: SHRP-A-645; National Research Council: Washington, DC, USA, 1993.

Disclaimer/Publisher’s Note: The statements, opinions and data contained in all publications are solely those of the individual author(s) and contributor(s) and not of MDPI and/or the editor(s). MDPI and/or the editor(s) disclaim responsibility for any injury to people or property resulting from any ideas, methods, instructions or products referred to in the content.